

Article

Evaluation of the Performance of the WRF Model in a Hyper-Arid Environment: A Sensitivity Study

Rachid Abida ^{1,*}, Yacine Addad ¹, Diana Francis ², Marouane Temimi ³, Narendra Nelli ²,
Ricardo Fonseca ², Oleksandr Nesterov ¹ and Emmanuel Bosc ⁴

¹ Emirates Nuclear Technology Center (ENTC), Department of Nuclear Engineering, Khalifa University of Science and Technology, Abu Dhabi P.O. Box 127788, United Arab Emirates; yacine.addad@ku.ac.ae (Y.A.); oleksandr.nesterov@ku.ac.ae (O.N.)

² Environmental and Geophysical Sciences (ENGEOS) Laboratory, Khalifa University of Science and Technology, Abu Dhabi P.O. Box 127788, United Arab Emirates; diana.francis@ku.ac.ae (D.F.); narendra.nelli@ku.ac.ae (N.N.); ricardo.fonseca@ku.ac.ae (R.F.)

³ Department of Civil, Environmental and Ocean Engineering (CEOE), Stevens Institute of Technology, Hoboken, NJ 07030, USA; mtemimi@stevens.edu

⁴ Federal Authority for Nuclear Regulation (FANR), Abu Dhabi P.O. Box 12778, United Arab Emirates; emmanuel.bosc@fanr.gov.ae

* Correspondence: rachid.abida@ku.ac.ae

Abstract: Accurate simulation of boundary layer surface meteorological parameters is essential to achieve good forecasting of weather and atmospheric dispersion. This paper is devoted to a model sensitivity study over a coastal hyper-arid region in the western desert of the United Arab Emirates. This region hosts the Barakah Nuclear Power Plant (BNPP), making it vital to correctly simulate local weather conditions for emergency response in case of an accidental release. We conducted a series of high-resolution WRF model simulations using different combinations of physical schemes for the months January 2019 and June 2019. The simulated results were verified against in-situ meteorological surface measurements available offshore, nearshore, and inland at 12 stations. Several statistical metrics were calculated to rank the performance of the different simulations and a near-to-optimal set of physics options that enhance the performance of a WRF model over different locations in this region has been selected. Additionally, we found that the WRF model performed better in inland locations compared to offshore or nearshore locations, suggesting the important role of dynamical SSTs in mesoscale models. Moreover, morning periods were better simulated than evening ones. The impact of nudging towards station observations resulted in an overall reduction in model errors by 5–15%, which was more marked at offshore and nearshore locations. The sensitivity to grid cell resolution indicated that a spatial resolution of 1 km led to better performance compared to coarser spatial resolutions, highlighting the advantage of high-resolution simulations in which the mesoscale coastal circulation is better resolved.

Keywords: hyper-arid region; Barakah nuclear power plant; WRF model; physical parametrizations; station nudging; statistical evaluation



Citation: Abida, R.; Addad, Y.; Francis, D.; Temimi, M.; Nelli, N.; Fonseca, R.; Nesterov, O.; Bosc, E. Evaluation of the Performance of the WRF Model in a Hyper-Arid Environment: A Sensitivity Study. *Atmosphere* **2022**, *13*, 985. <https://doi.org/10.3390/atmos13060985>

Academic Editor: Branko Grisogono

Received: 17 May 2022

Accepted: 15 June 2022

Published: 18 June 2022

Publisher's Note: MDPI stays neutral with regard to jurisdictional claims in published maps and institutional affiliations.



Copyright: © 2022 by the authors. Licensee MDPI, Basel, Switzerland. This article is an open access article distributed under the terms and conditions of the Creative Commons Attribution (CC BY) license (<https://creativecommons.org/licenses/by/4.0/>).

1. Introduction

The United Arab Emirates (UAE) is situated in a hyper-arid region on the north coast of the Arabian Peninsula and is adjacent to the Arabian Gulf, a shallow warm water body [1]. Hyper arid regions are fragile climatic regions that are, according to climate projections, expected to expand in a warmer world [2] and may experience more frequent severe weather conditions in the future [3]. It is therefore vital that regional weather forecasts and regional climate simulations correctly simulate essential surface meteorological quantities that characterize extreme events, and in particular, surface temperature, humidity, wind, and precipitations in such regions. However, model verification and sensitivity studies in

the context of a hyper-arid environment, like that of the UAE, have not been extensively addressed in the literature.

The target region of the present study is the coastal hyper-arid region in the western desert of the UAE. This particular region is of great importance as it hosts the Barakah Nuclear Power Plant (BNPP), the first commercial nuclear power plant in the Arabian Peninsula. This makes it also imperative to correctly simulate local weather conditions in this hyper-arid region for emergency response in case of an accidental release. The BNPP is an important component of the UAE's efforts to diversify its energy resources. Being located in a hyper-arid region, the environment around the nuclear power plant has unique characteristics compared to those of other sites, as it has an arid ground surface with low surface roughness [4], relatively flat terrain, extremely low precipitation [5,6], relatively high humidity with the presence of radiation fog during the cold season [7,8], intense solar radiation, and high temperature in the daytime during summer [9], sea/land breeze activity and frequent dust storms [10,11].

In the event of an accidental release of radionuclides into the atmosphere from BNPP, 3D Atmospheric Transport and Dispersion Models (ATDMs) would be used for dispersion calculations to model the consequences and to assist in determining appropriate countermeasures. However, besides uncertainties originating from the source term and parameterization in such models, an accurate representation of local weather conditions around the site is needed for a reliable dispersion simulation (e.g., Abida and Bocquet, 2009) [12]. Local weather conditions, particularly wind field patterns and boundary layer structure, determine the transport of a radioactive plume in the atmosphere, as well as its vertical and horizontal expansion [13,14]. For example, when the prevailing winds blow continuously in one direction, generally the radioactive materials are concentrated downwind from the source. By using a machine learning approach to characterize radionuclide dispersion from the Fukushima Daiichi accident release, Yoshikane and Yoshimura [15] pinpointed that radioactive plume directions and extensions can be estimated effectively by wind patterns. In a second study, Yoshikane et al. [16] showed that nocturnal local wind patterns around the Fukushima site had played a notable role in the long-distance transport of radioactive plumes. Thus, reliable meteorological forecasting representing local circulation and physical processes at a high resolution around the nuclear site is vital for emergency radionuclide monitoring.

High-resolution 3D non-hydrostatic numerical simulations with different physics parameterizations have been increasingly used to better understand various driving physical mechanisms for local meteorological phenomena. In opposition to coarse resolution simulations with convective parameterization, non-hydrostatic models have the advantage of resolving convection overturning explicitly. In particular, the state-of-the-art mesoscale model; Weather Research and Forecasting Model (WRF) is widely used to explore the formation and evolution of many local meteorological features, such as sea/land breeze circulation, and sea/land fog [17–24].

The WRF model incorporates complete physics for convection, boundary-layer turbulence, radiation, and land-surface processes, which play an important role in capturing the detailed evolution and structure of different atmospheric systems (e.g., Powers et al., 2017) [25]. For instance, Planetary Boundary Layer (PBL) turbulence diffusion plays a major role in the evolution of the lower atmosphere. Particularly, it drives atmospheric dispersion and its transport and deposition [26]. Thus, in addition to other important physical schemes, PBL parameterization schemes are particularly essential for accurate simulations of turbulence, wind components, and air pollution in the lower part of the atmosphere [27–29].

The WRF model has a large amount of available physical schemes, which makes it a suitable tool to thoroughly investigate physical processes under various land and atmospheric conditions. This large variability can help to explore which processes play a more dominant role in particular weather situations. However, it is worth mentioning that physical schemes present a principal source of uncertainty in high-resolution weather simu-

lations [30]. Hence, it is crucial to find an optimal combination of different physical options that reduce this source of uncertainty and subsequently improve the modeled results.

A variety of sensitivity studies have been carried out using the WRF model for investigating the performance of the various available physical parameterizations in accurately simulating weather conditions in varied geographic regions. All these studies have emphasized the role of the choice of the appropriate physical options to improve the model skill score for different applications [28,31–33]. For example, Yang et al. [24], in their WRF sensitivity study, pointed out that, with appropriate initial conditions, the PBL scheme, and microphysics scheme are the most important for sea fog formation and evolution. Carvalho et al. [34], Dzebre et al. [35], Chadee et al. [36] conducted sensitivity studies by varying different physical options in the WRF model to assess potential wind resources at different sites. Tyagi et al. [37], Boadh et al. [38], using the WRF model, analyzed the sensitivity of PBL schemes in simulating boundary layer flow parameters.

Nevertheless, there are very few sensitivity studies over the UAE regions. One was carried out by Chaouch et al. [18] to analyze the sensitivity of the WRF model to planetary boundary layer (PBL) schemes during fog conditions around Abu Dhabi airport and only used inland station observation to assess the performance of the model. The authors stressed that Local PBL schemes showed better performance compared to non-local schemes. On a larger scale, Taraphdar et al. [39] conducted a sensitivity study to assess the impact of physical parameterizations and model resolution on precipitation simulations over the UAE and the Middle East at the convective gray-zone resolution.

Moreover, it should be noted that non-hydrostatic short-scale simulations are known to be highly case-specific and geographically dependent (e.g., Yu et al., 2014) [40]. Commonly, all previous sensitivity studies using the WRF model showed that the performance of the model changes with different physical schemes and varies when the study region is changed. Thus, choosing the best set of physics options for the region and period under consideration is an essential step for calibrating the model simulations.

In this regard, the focus of the present work was to carry out a sensitivity study over the coastal hyper-arid region of the UAE where the BNPP is located. This study aimed to quantify the uncertainty in the WRF model using different physical schemes. To this end, various parameterization schemes were tested to determine the best combination for the forecasting of realistic boundary layer meteorological parameters, which are critical for dispersion calculations. The lack of a comprehensive evaluation of meteorological models in hyper-arid and coastal regions such as the BNPP site fosters the need to conduct such a thorough evaluation. The schemes that were investigated in this study included the planetary boundary layer (PBL), land-surface (LS), radiation, and microphysics (MP). WRF model simulations were performed with a 1 km horizontal resolution around BNPP, and the results were compared against available in-situ surface measurements, offshore, nearshore, and inland, at 12 stations distributed within a radius of 150 km around BNPP. The use of offshore observations, to our knowledge, adds to previous sensitivity studies in the region, such as that of Chaouch et al. [18], which focused on inland processes. The present study period covered the months of January and June 2019, which were representative of the prevailing winter and summer weather conditions at the site, respectively. Eventually, this work should lead to improving WRF forecasting performance around the BNPP site, which is essential for modeling atmospheric radionuclide dispersion.

2. Materials and Methods

2.1. Study Area and In-Situ Measurements

BNPP is a coastal desert site located in the Al Dhafra region of the Emirate of Abu Dhabi on the Arabian Gulf. Besides being in a hyper-arid region, BNPP is subject to land and sea breezes occurring daily. These mesoscale wind circulations are generated by local-thermally induced winds due to the contrast in heat capacities of land and seawater along the coastal lines. For instance, onshore winds carry maritime air masses towards the site during the night and early morning with a shallow maritime boundary layer. When reach-

ing the coast, an internal boundary layer develops and increases in depth progressively during daytime and as it moves inland. It is worth recalling that these mesoscale atmospheric wind circulations present important issues for coastal air environments because of their significant role in the transport and dispersion of air pollution [41].

Figure 1 shows the study area within a radius of 150 km from the nuclear site, represented by the innermost WRF domain. The available surface in-situ measurements are collected from twelve surface weather stations distributed at different distances from BNPP. Eleven of them are part of the UAE National Meteorology Center's (NCM) observing system network. The remaining one is a land-based 60-m weather tower operated by Nawah Energy Company in the UAE. Barakah NCM station and Nawah weather tower are located east-southeast of BNPP at distances of approximately 3.8 km and 1.2 km, respectively.

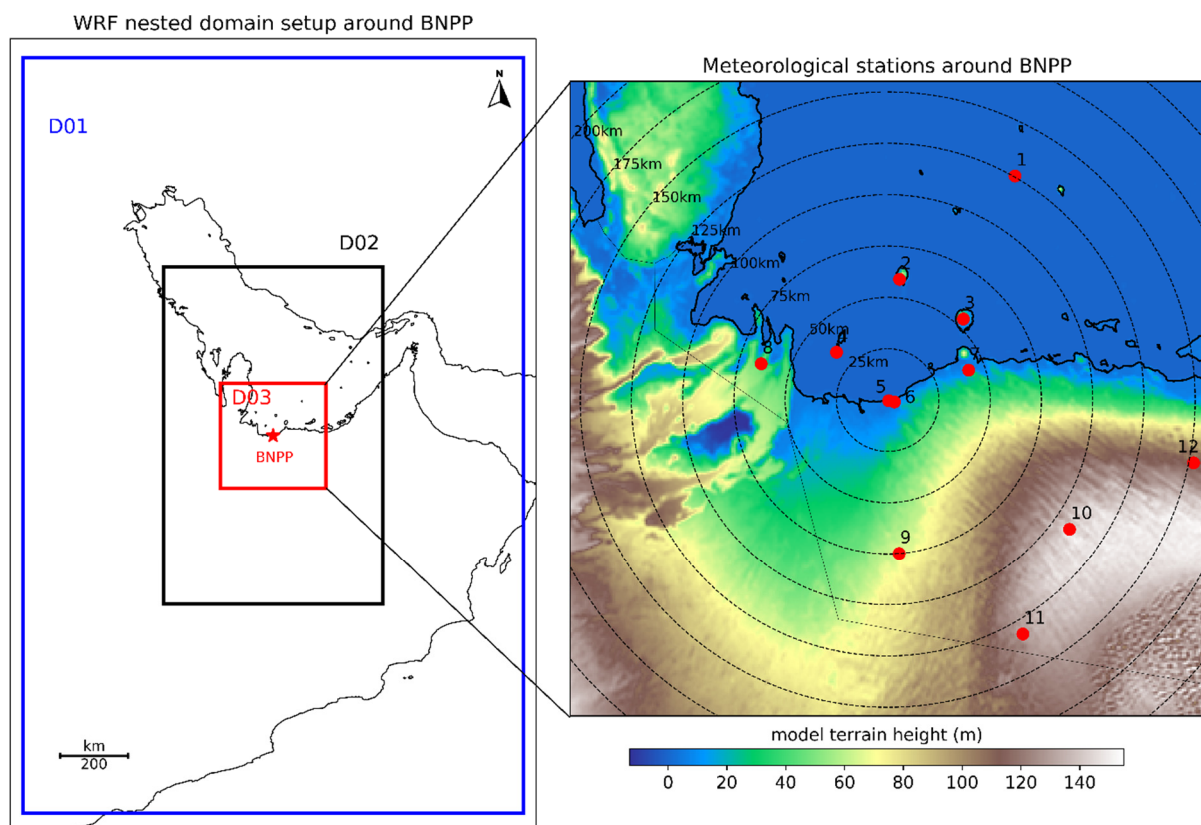


Figure 1. Study area for the experiments. (Left) The WRF domain configuration consists of three telescoping nests centered at BNPP. The star symbol depicts the BNPP location. The outermost boundaries denote the parent grid (D01). D02 and D03 are the nested domains. (Right) Left panel is a zoom of the innermost domain showing the model terrain height along with the spatial distribution of the 12 surface stations around BNPP. Each station is denoted by a red disk symbol and labeled by a number.

The meteorological parameters measured from NCM stations are air temperature and humidity at 2 m above the surface, wind speed and wind direction at 10 m, and solar radiation. This data is recorded every 15 min. While the weather tower gathers measurements every 10 min at three reading levels: air temperature and humidity at 2 m, temperature, wind speed, and wind direction at 10 m and 60 m. The overall considered stations are located in flat terrain environments, except inland stations which are located at higher elevations above sea level, as depicted in Figure 1 and Table 1.

Table 1. List of the weather stations used for the model validation.

Station ID	Station Name	Latitude	Longitude	Elevation (m)	Station Type	Distance from BNPP	Cardinal Direction from BNPP	Provider
1	Qarnen	24.9416	52.8497	32	offshore	125	NE	NCM
2	Dalma	24.4908	52.2913	25	offshore	58	NNE	NCM
3	SirBaniYas	24.3169	52.5977	14	offshore	54	NE	NCM
4	Yasat	24.1722	51.9883	12	offshore	34	NW	NCM
5	Nawah Tower	23.9599	52.2387	4	nearshore	1.2	ESE	NCM
6	Barakah	23.9552	52.2663	5	nearshore	3.8	ESE	Nawah
7	AlRuweis	24.0933	52.6227	32	nearshore	42	ENE	NCM
8	AlGhweifat	24.1211	51.6269	69	nearshore	64	WNW	NCM
9	Aljazeera	23.2911	52.2888	70	inland	75	S	NCM
10	Owtaid	23.3955	53.1027	180	inland	109	SE	NCM
11	Mukhariz	22.9347	52.8777	145	inland	132	SSE	NCM
12	MadinatZayed	23.6816	53.6986	118	inland	152	ESE	NCM

For this study, the in-site measurement stations around BNPP are categorized as follows: four offshore stations, four near-shore stations, and four inland stations. Table 1 gives the station names and their locations. Observations for January and June 2019 as representative months for winter and summer in the region were used for the present short-term validation study. It is worth mentioning that these data were also used to better constrain the initial conditions of the WRF model through the surface nudging technique.

2.2. Meteorological Model

The model used in this study to carry out the numerical simulations is the Advanced Research WRF (ARW) v4.2 [42], a largely used community mesoscale model developed by the National Center for Atmospheric Research (NCAR). It represents the current state of the science in mesoscale weather modeling. It consists of a Eulerian mass solver with fully compressible non-hydrostatic primitive equations. The model is terrain-following vertical coordinate with the top of the model being a constant pressure level. It uses the staggered Arakawa C-grid along with Runge-Kutta third-order scheme for the time integration. The model is conservative for scalars and incorporates multiple options for various physical parametrization schemes.

To better resolve local-scale atmospheric circulation around BNPP, the WRF model is designed with three two-way interactive nested domains of resolution 25 km, 5 km, and 1 km, and 45 unequally spaced sigma-pressure vertical levels. There are approximately 11 vertical levels below 1 km above-ground level. Figure 1 depicts the three telescoping nested domains centered on BNPP's location (23.9696° N, 52.2359° E). The parent domain (D01) consists of 61 × 91 grid points and covers the Arabian Gulf, Gulf of Oman, portions of the Arabian Sea, the Empty Quarter, and parts of Iraq and Iran. The second inner domain (D02) comprises 131 × 201 grid points and covers large portions of the Arabian Gulf and Empty Quarter desert. The innermost domain (D03), which represents the study area, consists of 311 × 311 grid points and encompasses a region within a radius of 150 km from BNPP.

Meteorological analysis from the National Centre for Environmental Prediction (NCEP) Global Forecast System (GFS) with a horizontal spatial resolution of 0.25° and with a time resolution of 6 h were used to provide initial and boundary conditions to WRF simulations. MODIS 20 classification category land-use data were used for generating topography

and land use with a spatial resolution of 30 arc-second (~900 m). Besides atmospheric fields, time-varying analyzed SSTs (Sea Surface Temperature) within NCEP GFS were also supplied to the model. Once initialized each day, the SST field was kept constant throughout the model integration period. The integration time step on the parent domain was set to 120 s. Table 2 summarizes the modeling domains and model configuration.

Table 2. WRF model configuration around BNPP.

Non-Hydrostatic Model	Advanced Research WRF v4.2		
Driving data	NCEP GFS at 0.25° spatial and 6-hourly temporal resolution, and 32 pressure vertical levels. Time-varying analyzed GFS SST. Held constant during the model integration time period		
Land use data	20-category MODIS at 30 arc-seconds		
Geographical projection scheme	Mercator		
Horizontal grid system	Arakawa-C grid		
Horizontal resolution (km)	25	5	1
Domain size (grid-points)	61 × 91	131 × 201	311 × 311
Vertical resolution	45 terrain-following sigma-pressure vertical levels		
Integration time step	120 s		
Time integration scheme	3rd order Runge-Kutta scheme		
Spatial differencing scheme	6th order center differencing		
Spin-up time period	12 h		
Integration time period	36 h		

2.3. Experimental Sensitivity Design

The WRF model incorporates multiple options for various physical parametrization schemes. Finding a close-to-optimal set of physical options which ensures WRF forecasting simulations with sufficient accuracy around BNPP is crucial. However, performing an exhaustive combinatorial optimization of the physical parameters of WRF was outside the scope of this study due to the large number of scheme combinations that need to be tested (there are more than 5000 possible combinations in WRF v4.2) which is a very challenging task [43]. In the present work, we created 13 WRF experiments based on trial runs and considering the most relevant physical settings based on previous studies [17,18,33,34,36–38,43,44]. The scheme types investigated were boundary layer, land surface, radiation, and microphysics.

Overall, we used six PBL parameterization schemes. These schemes have different formulations for mixing the boundary layer and for PBL height determination, which affect the reconstruction of dispersion and ground concentrations of various pollutants [45]. There are four TKE closure schemes—Mellor-Yamada-Nakanishi-Niino level-2.5 model (MYNN2.5) [46], Mellor-Yamada-Nakanishi-Niino level-3 model (MYNN3) [46], Mellor-Yamada-Janjic (MYJ) [47], Quasi-Normal Scale Elimination-Eddy Diffusivity Mass Flux (QNSE-EDMF) [48]—and two first-order closure schemes, Yonsei University (YSU) [49], asymmetric convective model 2 (ACM2) [50]. We considered three parameterization schemes for the microphysics: WRF Single Moment 3 Class (WSM3-Class), Purdue Lin scheme, and Thompson graupel scheme. The main difference between the microphysics schemes is the amount of water species that they consider and their size distribution and mixing ratios. For radiation, we considered Dudhia [51] and RRTMG [52] for shortwave radiation schemes, and RRTM [53], RRTMG for longwave radiation schemes. RRTM and RRTMG are similar but show slight differences in the microphysics interactions and RRTMG has a higher background CO₂ concentration.

For the surface layer, we included five schemes: Revised MM5 Monin-Obukhov [54], Mellor-Yamada-Nakanishi-Niino (MYNN), Quasi-Normal Scale Elimination (QNSE), Monin-Obukhov, and Pleim Xiu scheme. Regarding land surface physics, we considered three options: 5-layer thermal diffusion, unified Noah land-surface model, and Noah-MP land-surface model. For cumulus parametrization, we used two schemes: Betts-Miller-Janjic (BMJ) and Kain-Fritsch (new Eta) schemes. For the description and physical working principle of each of the chosen schemes, one can refer to the WRF user guide manual (chapter 5). Table 3 summarizes the constructed experiments. Note that Experiment 13 (EXP13) has the same physical parameters as Experiment 8 (EXP08) except that it includes, in addition, a topographic correction for surface winds to represent the additional drag of the sub-grid topography.

Table 3. Physical scheme options used for the different 13 WRF experiments.

Simulation ID	Microphysics	LW RAD	SW RAD	Surface Layer	Land Surface	PBL	Cumulus
EXP01	WSM 3-class	RRTM	Dudhia	Revised MM5	Thermal Diffusion	YSU	BMJ
EXP02	Thompson graupel	RRTMG	RRTMG	MYNN	Unified Noah Model	MYNN 2.5	BMJ
EXP03	Thompson graupel	RRTMG	RRTMG	Revised MM5	Unified Noah Model	YSU	Kain-Fritsch
EXP04	Thompson graupel	RRTM	RRTMG	QNSE	Unified Noah Model	QNSE-EDMF	Kain-Fritsch
EXP05	Thompson graupel	RRTM	RRTMG	Monin-Obukhov	Unified Noah Model	MYJ	Kain-Fritsch
EXP06	Thompson graupel	RRTM	RRTMG	MYNN	Unified Noah Model	MYNN3	Kain-Fritsch
EXP07	Thompson graupel	RRTM	RRTMG	Revised MM5	Thermal Diffusion	YSU	Kain-Fritsch
EXP08	WSM 3-class	RRTM	RRTMG	Revised MM5	Thermal Diffusion	YSU	Kain-Fritsch
EXP09	Perdue Line	RRTM	Dudhia	QNSE	Unified Noah Model	QNSE-EDMF	Kain-Fritsch
EXP10	Perdue Line	RRTM	Dudhia	QNSE	Thermal Diffusion	QNSE-EDMF	Kain-Fritsch
EXP11	Thompson graupel	RRTM	RRTMG	Pleim Xiu	Unified Noah Model	ACM2	Kain-Fritsch
EXP12	Thompson graupel	RRTM	RRTMG	Revised MM5	Noah-MP Model	YSU	Kain-Fritsch
EXP13	WSM 3-class	RRTM	RRTMG	Revised MM5	Thermal Diffusion	YSU with topo_wind option enabled	Kain-Fritsch

For every single experiment, we performed a 36-h model simulation for each calendar day of January and June 2019. Explicitly the model was initialized 12 h before 00 UTC each day. It should be noted that the model initialization time has an impact on the simulated results as was demonstrated, for example, in Chaouch et al. [18]. The spin-up period was set at 12 h, which was assumed to be long enough for allowing the model to generate sufficient mesoscale information that is absent from the coarser boundary conditions [55]. Moreover, during the first 6 h of the spin-up period, the model was integrated with digital filter initialization (DFI) activated. This helped to further reduce the initial model imbalance.

For each single simulation experiment, we created a twin experiment in which the station nudging technique was applied in the innermost domain, but only during the spin-up period. Station nudging is an option of the WRF 4D data assimilation (FDDA) system, that consists in keeping the model close to the observations during the integration period. The nudged surface variables were air temperature and relative humidity at 2 m, and horizontal wind components at 10 m. The nudging was set to spread the influence of innovations calculated from surface observations throughout the PBL with decreasing weight with height. The observations were fed into the model every 15 min. The strength of the nudging term was set to gradual decrease over the pre-forecast period to minimize the noise that might be caused by turning the station nudging off abruptly. It is worth mentioning that for all the conducted simulations, cumulus parametrization was enabled only in the outermost domain (25 km) while microphysics were activated only in the inner nests (5 km, and 1 km).

2.4. Error Metrics for Model Validation

The instantaneous hourly data for the essential meteorological surface parameters obtained from the different model experiments were used to compare against the available surface meteorological data to assess the model performance for each physical configuration. Namely, the model-simulated air temperature and relative humidity at 2 m height, wind speed, and wind direction at 10 and 60 m heights, along with solar radiation flux were interpolated to the station locations and compared to the corresponding observation data using different statistical metrics.

Various statistical metrics can be used for model-to-observation quantitative comparison. However, there is no special error statistic that encapsulates all aspects of interest because each statistical metric gives a different piece of information. For that reason, it is important to use different error statistics and to understand the type of information they might provide. For this study, different performance statistics were computed to rank the physical combinations for the different conducted simulations. These error statistics characterize the strength of correlation, systematic error, and random error [35,56]. The statistic considered are detailed as follow:

- the unbiased Pearson correlation coefficient (ρ)
- the Root Mean Square Error (*RMSE*)
- the Mean Absolute Error (*MAE*)
- the Mean Bias (*MB*)
- the Standard Error (*STDE*)

The correlation coefficient (ρ) is a measure of the linear correlation between the model and observations and is calculated as:

$$\rho = \frac{1}{(N-1)} \sum_{i=1}^N \left(\frac{M_i - \bar{M}}{\sigma_M} \right) \left(\frac{O_i - \bar{O}}{\sigma_O} \right),$$

where M_i , O_i represent model and observation time series, respectively, \bar{M} , \bar{O} are the arithmetic means of the model and observation, σ_M , σ_O are the standard deviations for model and observation, and N stands for the number of data points in the series.

The *RMSE* and *MAE* are a measure of the model's prediction accuracy, and determine the mean error between the model and observation regardless of whether it is an over or underestimate. Notice that *RMSE* is very sensitive to larger errors, while *MAE* gives the same weight to all individual errors. *RMSE* and *MAE* are calculated as:

$$RMSE = \left(\frac{1}{N} \sum_{i=1}^N \Delta_i^2 \right)^{0.5}, \quad MAE = \frac{1}{N} \sum_{i=1}^N |\Delta_i|,$$

where $\Delta_i = M_i - O_i$, stands for individual errors.

MB is a measure of the systematic error and determines whether the model is over or underpredicting. It is calculated as:

$$MB = \frac{1}{N} \sum_i^N \Delta_i.$$

STDE is a measure of the random error and is used to evaluate the spread in the prediction error. A smaller value of *STDE* is preferred. Low *STDEs* can be taken as an indication of consistency in model performance [34]. *STDE* is calculated from *RMSE* and *MB* as:

$$STDE = \left(RMSE^2 - MB^2 \right)^{1/2}$$

Note that since the wind direction is a circular parameter ($0^\circ = 360^\circ$) and not a linear one, and the absolute differences between the model and observations, $|\Delta_i|$, should not exceed 180° in modulus. Thus *RMSE*, *MAE*, *MB*, and *STDE* for wind direction are calculated by using a different formulation for the differences Δ_i [57]:

$$\Delta_i = \left\{ \begin{array}{l} M_i - O_i \text{ if } |M_i - O_i| < 180^\circ \\ (M_i - O_i) * \left(1 - \frac{360^\circ}{|M_i - O_i|} \right) \text{ if } |M_i - O_i| > 180^\circ \end{array} \right\}$$

The correlation between the modeled and measured wind directions are determined with a Circular Correlation Coefficient [58].

Furthermore, to compare and rank the conducted WRF experiments, we computed another statistical metric (*MSS*) according to [59] which quantifies the model skill score as follows:

$$MSS = \rho_{scaled} + (1 - RMSE_{scaled}) + (1 - MAE_{scaled}) + (1 - STDE_{scaled}) + (1 - |MB_{scaled}|), \quad (1)$$

where the metrics were scaled as:

$$X_{scaled} = \frac{X_l - X_{min}}{X_{max} - X_{min}}$$

For a particular metric *X*, and a given station, X_l spans all the physical configurations. X_{max} and X_{min} refer to maximum and minimum values for that metric. *MSS* ranges from 0 to 5. A model experiment with higher *MSS* is ranked as the best physical combination, and vice versa. The statistical metrics were calculated for the various surface meteorological parameters using hourly data for January and June 2019.

3. Results and Discussion

3.1. Overall Model Performance Assessment

The goal of this section is to conduct a statistical evaluation to assess the overall performance of each model experiment around BNPP. To this end, the model-generated surface meteorological variables such as air temperature (T2), relative humidity (RH2) at 2 m, and wind speed (WS) and wind direction (WD) at 10 m above the ground are directly compared with the surface meteorological observations from the 12 ground-based stations available within a radius of 150 km from Barakah nuclear site. This allows us to determine how the WRF model performs at different locations around the nuclear site for a given physical setting. Particularly, at offshore, nearshore, and inland locations. The statistical metrics were calculated using hourly data for June 2019 and January 2019 separately. Each calculated metric was represented in a matrix form to summarize the model to observation comparison for the 13 model experiments. In this metric matrix, the columns depict the 13 model experiments, and the rows represent the 12 ground-based stations. These are ordered later based on their types as described in Table 1, and on their distances from BNPP, so that the onshore stations which are far from the site are represented in the upper rows, while the inland stations are represented in the bottom rows. The statistical metric matrix is built in this way to help diagnose any sea to land transition in WRF model performance. In this section, we only show the results for June 2019, since the computed statistics for January 2019 led to the same main conclusions.

Figures 2–4 show, respectively, the correlation metric matrix, the mean bias metric matrix, and the mean absolute error metric matrix calculated using June 2019 hourly data for the surface variables: T2, RH2, WS and WD at 10 m. The first interesting finding that we can spot on Figures 2 and 4

is the presence of a noticeable sign of a sea-to-land transition in the model’s performance when inspecting the ρ and MAE metric matrices. This transition is particularly more marked for 2 m air temperature and relative humidity. Notice that this signature is less stressed in 10 m wind speed and is not prominent in 10 m wind direction. All the performed model simulations exhibited this signature with relatively different strengths. Generally, we observed that, regardless of the used set of physical options, the inland locations were better simulated than onshore or nearshore locations.

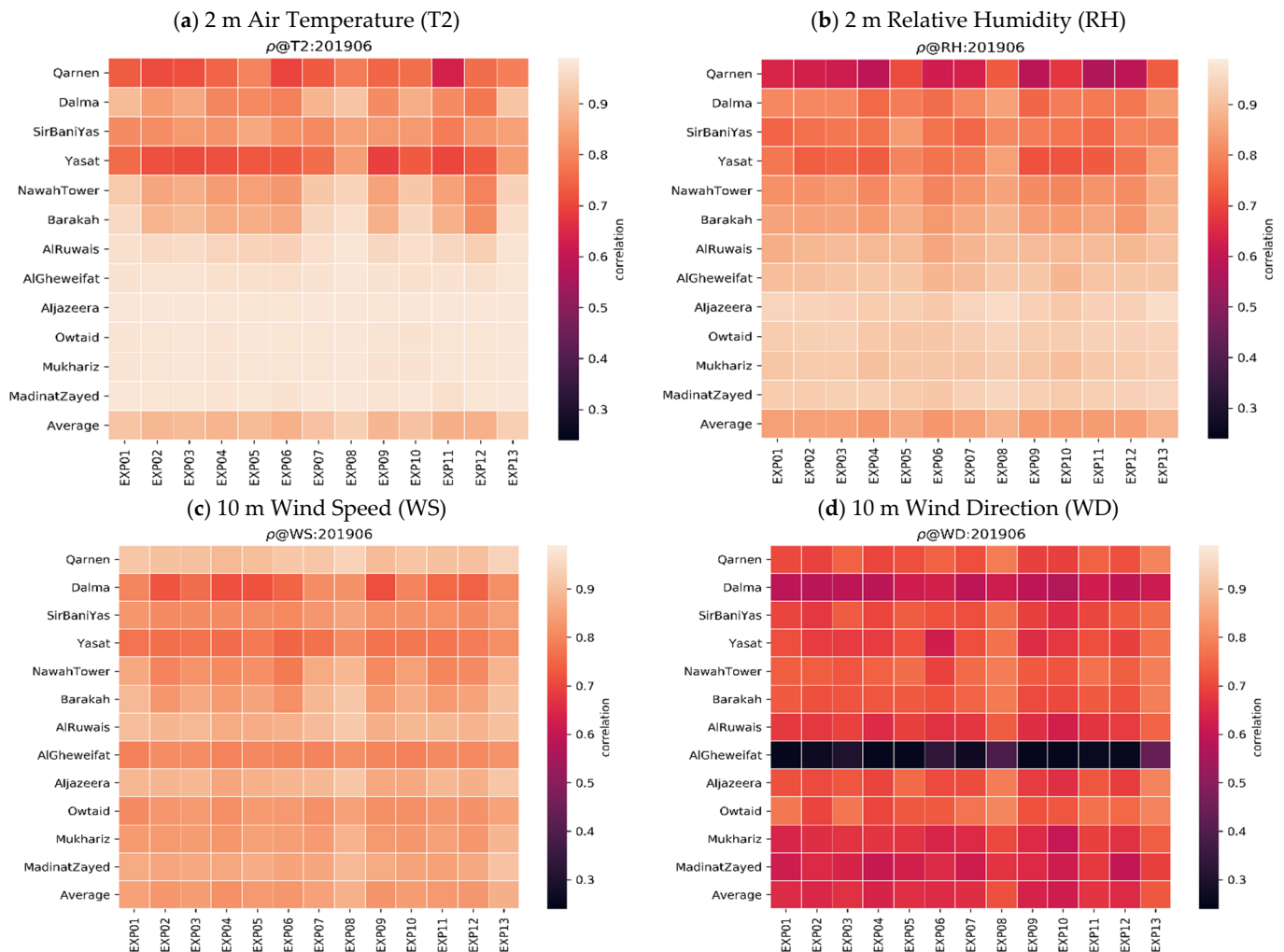


Figure 2. Correlation coefficient (ρ) between station data and the conducted model experiments calculated using June 2019 hourly data for the surface parameters 2 m air temperature (T2) and relative humidity (RH2), wind speed (WS), and wind direction (WD) at 10 m above the ground. The last lines of the heatmaps show average values over all stations.

This result is in line with previous WRF model evaluation studies, particularly, with the one carried out by Tyagi et al. [37] aiming to analyze the sensitivity of different boundary layer parameterization schemes in the WRF model over southern Italy. This result pinpoints that the physical processes in the marine boundary layer are not sufficiently resolved by the WRF model compared to its performance over land. This could be explained by the fact that much of the development of PBL schemes has been focused on land rather than over sea, in part due to the scarcity of marine observations. In addition to this, another parameter that could impact the performance of the model at onshore and nearshore locations is the SST forcing field. This is kept constant throughout the model integration period, and might partly reduce the quality of model prediction over sea locations because SSTs in this region can vary by up to 1.5 °C on average between the morning and evening periods, as pointed out by Nesterov et al. [1]. Needless to say, sea surface roughness length (z_0) has a direct impact on the quality of sea surface wind simulations. In the WRF model, z_0 is calculated using the Charnok formulation [60]. Lee et al. [61] by coupling WRF single-column model with

a Kalman filter, pointed out that an optimal estimation of z_0 can improve offshore wind forecasts by 4–22%.

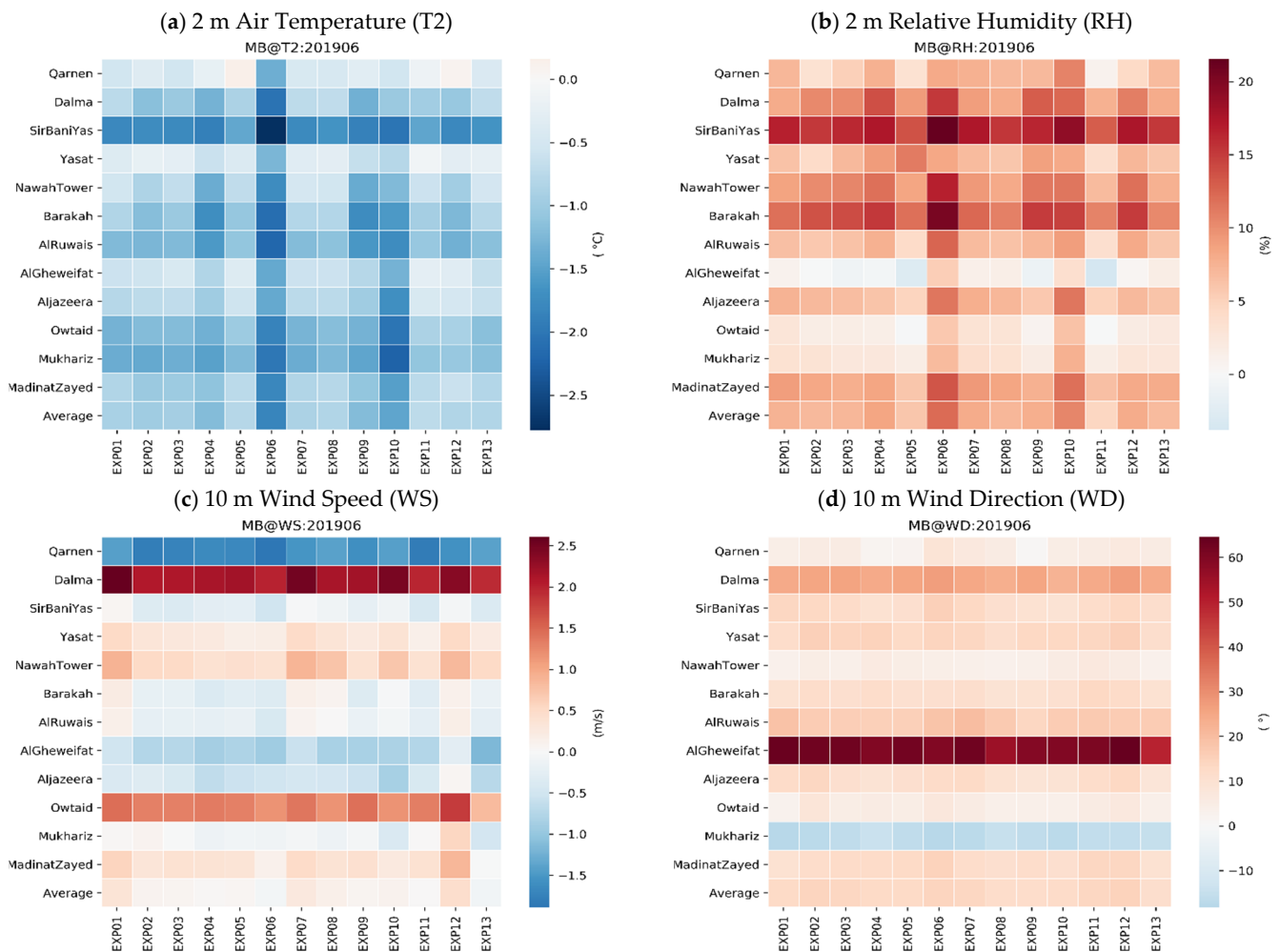


Figure 3. Mean Bias metric (*MB*) between station data and the conducted model experiments calculated using June 2019 hourly data for the surface parameters 2m air temperature (*T2*) and relative humidity (*RH*), wind speed (*WS*), and wind direction (*WD*) at 10 m above the ground. The last lines of the heatmaps show average values over all stations.

Additionally, it should be noted that high-resolution non-hydrostatic simulations are known to be highly case and geographically dependent. This general statement is confirmed by the calculated metric matrices which show that the performance of the model changes with different physical schemes and varies from one location to another. This means that an optimal combination of physical options for a particular location might not be a good choice for another location.

The correlation maps (Figure 2) show that all the experiments reproduced the variability of the observed data reasonably well since the proportion of the explained variance (ρ^2) by the model was between 40 and 92%. However, for the 10 m wind direction parameter, we noticed that all experiments failed to capture the observed variability at Al Ghweifat station (ID 8) where higher values of *MAE* and *MB* (Figures 3d and 4d) in all experiments compared to other stations were reported. This shortcoming is likely related to an existing artifact in the wind direction measurements, as none of the different model configurations led to a realistic reproduction of the observed data at this peculiar station.

Interestingly, the mean bias metric matrix (Figure 3a) for the *T2* parameter highlights that the model, on average, had an overall cold bias with respect to the 12 weather stations (i.e., model-observation <0). All the experiments exhibited this inherently cold mean bias with relatively different magnitudes. This systematic cold bias is probably due to the higher longwave surface cooling rate in the PBL schemes compared to the observation (e.g., Fonseca et al., 2020) [62]. On the other hand, Figure 2b shows that

commonly all the model experiments simulated a higher magnitude of RH2. The overestimation of RH2 may be attributed to the model cold bias. For WS and WD parameters, we observe from Figure 3c,d that the model has a systematic mean bias that sign and magnitude vary with the station location and the physical settings.

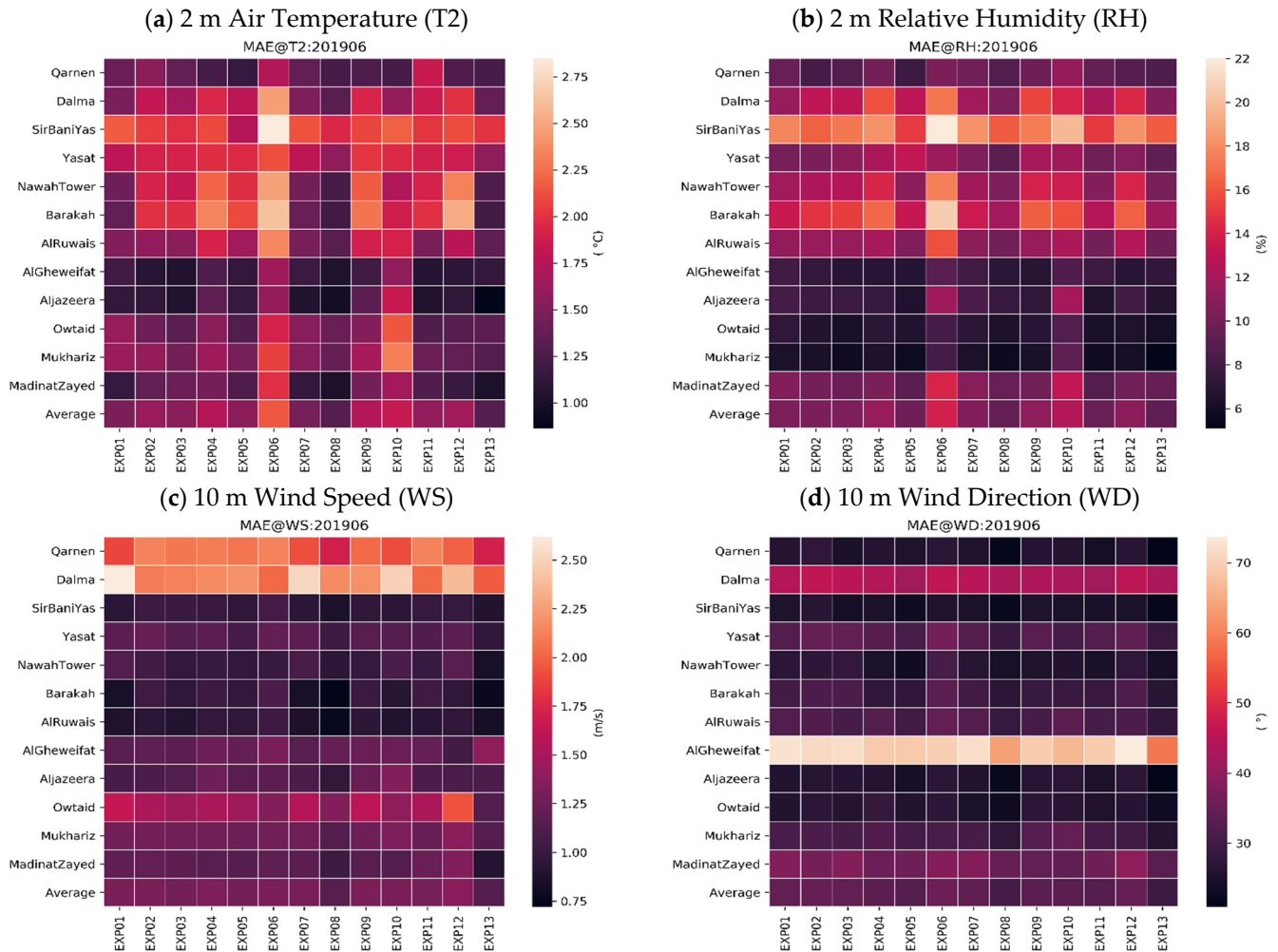


Figure 4. Mean Absolute Error (MAE) between station data and the conducted model experiments calculated using June 2019 hourly data for the surface parameters 2m air temperature (T2) and relative humidity (RH), wind speed (WS), and wind direction (WD) at 10 m above the ground. The last lines of the heatmaps show average values over all stations.

In addition, a joint analysis of the statistical metric matrices shows that the EXP01, EXP08, and EXP13 achieve better performance than all other experiments. In the subsequent sections, we illustrate how the ranking of the experiments is carried out. EXP08 utilizes WSM 3-class microphysics, RRTM for longwave radiation, RTTMG for shortwave radiation, Kain-Fritsch cumulus, YSU PBL, revised MM5 surface layer Monin-Obukhov, and thermal diffusion scheme. It should be noted that EXP13 has the same physical parameters as in EXP08 except that the topographic correction for surface winds to represent the additional drag of the sub-grid topography is activated in EXP13 but not in EXP08. EXP01 only differs from EXP08 in cumulus and shortwave radiation schemes. Instead, it uses Betts-Miller-Janjic (BMJ) cumulus scheme and Dudhia scheme for shortwave radiation.

3.2. Impact of Station Nudging

In this section, we investigate the added value of dynamic initialization through station nudging and horizontal resolution on improving the model performance. Recall that for each single model simulation of the thirteen model experiments, a twin experiment having the same physical settings was created in which the station nudging technique was applied in the innermost domain. The

surface observations were taken into the model every 15 min. Station nudging was applied only over the spin-up period to allow mesoscale processes in the PBL to develop freely during the model integration time period. The benefit of station nudging on improving the model-to-observation statistics is measured by the quantity $100 * \left| \frac{m^*}{m} - 1 \right|$, where m, m^* stand for a given statistical metric calculated for the reference experiment and the one with station nudging, respectively. Here we only show the results obtained for June 2019 since the results calculated for January 2019 led to similar conclusions.

Figure 5 depicts the increase in correlation coefficient (ρ), and the decrease in the mean absolute error (MAE) for 2 m air temperature and 10 m wind speed. This figure demonstrates an overall positive impact of the surface station nudging in enhancing the model-to-observation statistics. Interestingly, for the 2 m air temperature parameter, we notice that the model corrections made through nudging are more pronounced on onshore and nearshore stations than on inland locations.

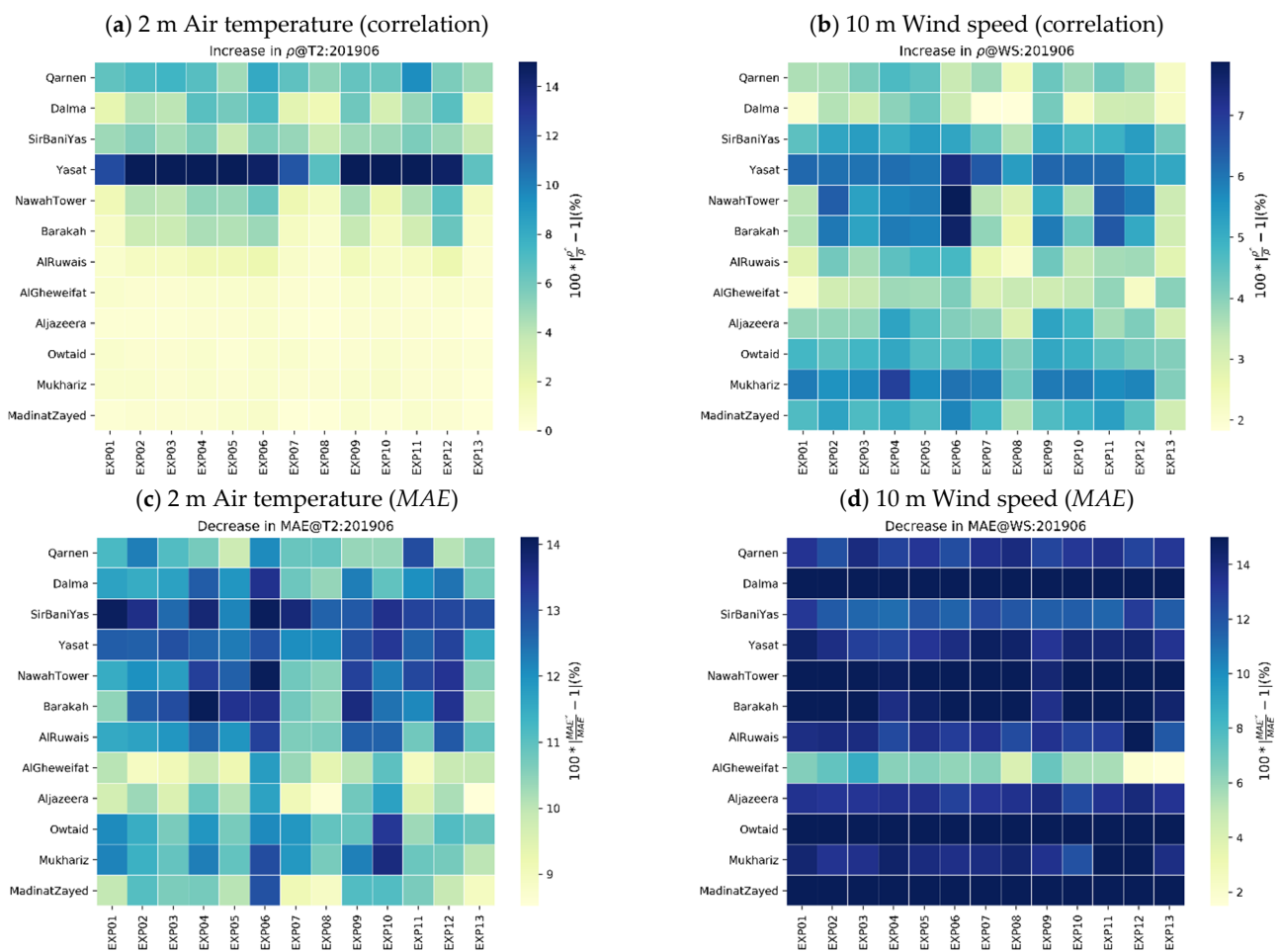


Figure 5. Impact of dynamic initialization through station nudging on model-to-observations statistics. (a,b) represent respectively the increase in the correlation for 2 m air temperature and 10 m wind speed; (c,d) depict the decrease in the mean absolute error for the same two surface parameters.

There was a small improvement in the correlation of less than 4% at inland sites, whereas at onshore and nearshore locations, we saw a noticeable increase in the correlation of around 6–14%. In addition, we observed an overall reduction in model error of about 8% to 14%, which was more marked at onshore and nearshore sites. This gain in the model performance at onshore and nearshore sites is explained by the fact that the model initially simulated 2 m air temperature with sufficient accuracy over land than over sea. Hence the corrections brought by the station nudging are more focused on sea sites. For 10 m wind speed, we observed an increase in the correlation by 2–8% and an overall decrease in the model error by 11–14%, except at Al Ghweifat station where the reduction was about 2–8%.

Finally, these results show that station nudging—especially when surface observations are assimilated into the model at high temporal frequency—has the potential to mitigate the initial model imbalance by extracting the mesoscale information from the surface stations, and subsequently reduce the model errors of surface parameters. This finding agrees with other studies, and in particular, with that carried out by Dzebre et al. [35] to study the impact of nudging options on WRF surface wind simulation at a coastal site.

3.3. Sensitivity to Horizontal Resolution

In addition to the effect of surface nudging, we also investigated the impact of the horizontal resolution on model performance. To this end, we calculated three versions of the statistical metrics using the 1 km, 5 km, and 25 km model outputs of the EXP08 which seem to have, according to the findings mentioned in the previous section, the optimal combination of physical parameterization options. Figure 6 shows the correlation (ρ) and root mean square error (RMSE) for 2 m air temperature and 10 m wind speed parameters calculated for the twelve surface stations using June 2019 data. Results for January 2019 were similar and therefore are not shown. We observed a clear benefit of the high horizontal resolution on the model performance. The statistics calculated for a resolution of 1 km were much better than those calculated for the resolutions of 5 km and 25 km. Note that the statistics for the underlying resolutions get gradually better when moving from onshore towards inland stations. Particularly, over the onshore stations, Dalma, Qarnen, SirBaniYas, and Yasat, we observed a noticeable discrepancy in the values of the statistics between the high-resolution and the coarse-resolution. This is attributed to the fact that the coarse-resolution simulation is dominated by large-scale conditions that do not contain realistic vertical motions associated with mesoscale coastal circulations. Conversely, these characteristics are better represented in the high-resolution simulation. It is interesting to note that at Aljazeera station, located inland, there was a small difference in the performance of the model of the three resolutions. This could indicate that horizontal resolution has a low impact on model performance, especially in inland areas characterized by simple flat terrain and located far from the direct effect of the coast or elevated terrains.

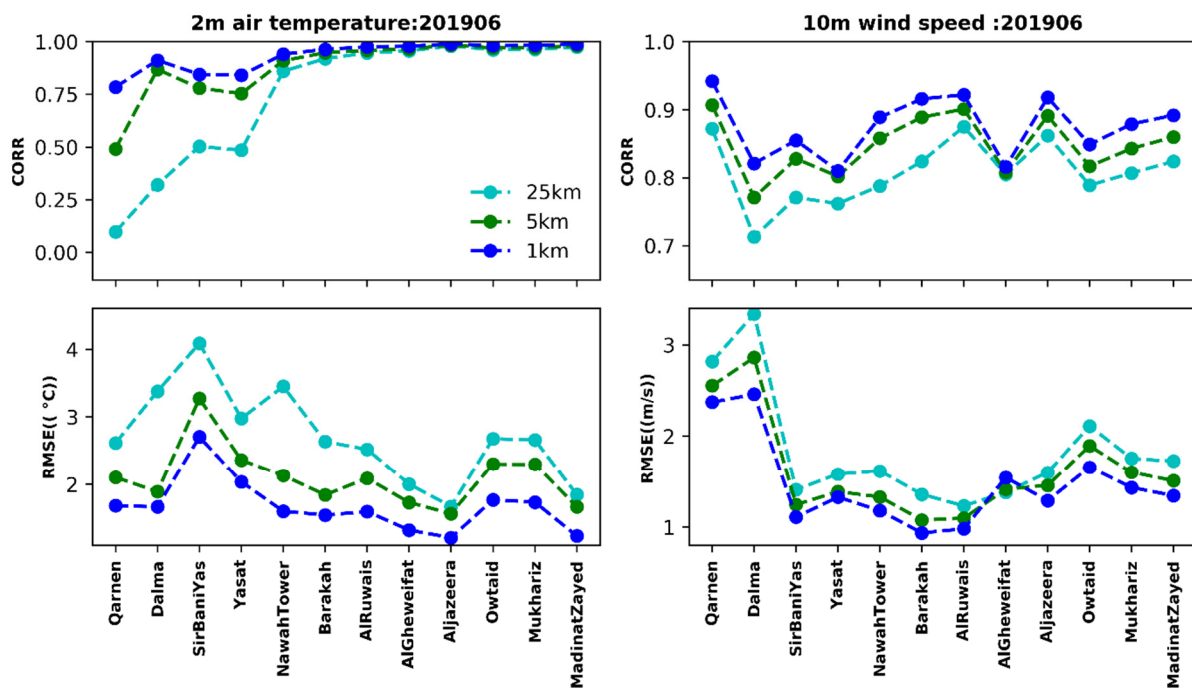


Figure 6. Impact of horizontal resolution on model performance. Panels show the correlation and RMSE between the model and the 12 stations. Statistics are calculated for T2 and WS using June 2019 data of the experiment EXP08 at spatial resolutions of 1 km, 5 km, and 25 km.

3.4. Statistical Model Evaluation at Barakah Station

The goal of this section is to present an intercomparison of the performance of the various model experiments near BNPP to choose the best combination of physical parametrization options which guarantee a better simulation of surface meteorological variables such as T2 (°C), RH (%),

WS (m/s), and WD (°). To this end, the statistical model performance indicators were calculated using the hourly in-situ observations at Barakah station which is in the east-southeast of the nuclear site at 3 km (see Table 1 and Figure 1).

3.4.1. Air Temperature and Relative Humidity

Statistical evaluations for Barakah station for June and January 2019 are summarized, respectively, in Tables 4 and 5. For temperature, we can note that the EXP01, EXP08, and EXP13 simulations were satisfactory in terms of statistical evaluation because they reported the lowest values of *MB*, *RMSE*, *MAE*, and *STDE*, and the highest correlations with the observations. Notice that the statistics for January 2019 are slightly better than those for June 2019. In addition, we note that all model simulations with the different combinations of the physical parametrizations showed a cold bias, especially for June. Conversely, for January, we observed a warm bias except for EXP06, and EXP10 which reported a minor cold bias. For relative humidity, we noticed that the simulations EXP01, EXP08, EXP13, EXP11, and EXP12 showed better performance than the other simulations. All the model simulations indicated positive biases of about 10–20%. The values of the statistical metrics for January were much better than those calculated for June, which may be due to the more complex atmospheric circulation over the region during summer with the development of the Arabian Heat Low Fonseca et al., 2022 [63], the Intertropical discontinuity region [64] and sporadic localized convective systems [6].

Table 4. Statistical metrics calculated for June 2019 hourly data at Barakah station.

	EXP01	EXP02	EXP03	EXP04	EXP05	EXP06	EXP07	EXP08	EXP09	EXP10	EXP11	EXP12	EXP13
2 m Air Temperature (°C)													
ρ	0.954	0.883	0.895	0.865	0.871	0.861	0.947	0.964	0.878	0.948	0.878	0.813	0.962
<i>MB</i>	−0.836	−1.185	−1.037	−1.730	−1.076	−2.113	−0.816	−0.821	−1.754	−1.597	−0.935	−1.255	−0.802
<i>MAE</i>	1.363	1.988	1.973	2.339	2.096	2.629	1.396	1.208	2.273	1.880	1.991	2.519	1.219
<i>RMSE</i>	1.723	2.544	2.428	2.952	2.592	3.243	1.759	1.545	2.880	2.236	2.472	3.057	1.575
<i>STDE</i>	1.507	2.251	2.196	2.392	2.358	2.460	1.559	1.309	2.284	1.564	2.289	2.788	1.355
2 m Relative Humidity (%)													
ρ	0.854	0.848	0.854	0.836	0.870	0.832	0.863	0.887	0.843	0.837	0.858	0.828	0.890
<i>MB</i>	11.846	13.721	14.068	15.302	11.938	20.411	12.330	10.917	14.987	14.771	10.739	15.011	10.444
<i>MAE</i>	13.481	14.755	15.158	16.658	13.309	20.690	13.512	11.942	16.266	15.829	12.613	16.398	11.730
<i>RMSE</i>	17.424	17.712	17.994	19.614	15.952	23.614	17.301	15.276	19.249	19.578	15.668	19.444	15.040
<i>STDE</i>	12.778	11.201	11.218	12.271	10.580	11.875	12.136	10.684	12.080	12.850	11.409	12.360	10.823
10 m wind speed (m/s)													
ρ	0.891	0.829	0.860	0.836	0.854	0.820	0.888	0.916	0.836	0.869	0.836	0.850	0.906
<i>MB</i>	0.207	−0.208	−0.212	−0.375	−0.298	−0.347	0.162	0.09	−0.347	−0.031	−0.319	0.143	−0.17
<i>MAE</i>	0.840	1.033	0.960	1.024	0.974	1.097	0.844	0.721	1.016	0.915	1.033	0.963	0.771
<i>RMSE</i>	1.074	1.313	1.208	1.329	1.246	1.380	1.078	0.935	1.321	1.164	1.315	1.231	0.997
<i>STDE</i>	1.054	1.297	1.190	1.275	1.209	1.336	1.066	0.931	1.274	1.164	1.276	1.222	0.983
10 m wind direction (°)													
ρ	0.732	0.715	0.723	0.725	0.731	0.720	0.744	0.781	0.706	0.704	0.732	0.715	0.790
<i>MB</i>	10.028	11.989	11.080	11.983	10.522	10.909	11.483	9.624	10.253	10.581	13.394	12.331	9.787
<i>MAE</i>	30.293	31.569	31.459	27.635	27.559	33.349	30.198	26.950	28.781	28.858	28.568	31.763	26.379
<i>RMSE</i>	47.542	49.677	49.508	43.151	44.245	53.065	47.803	44.141	44.837	46.331	45.050	48.756	43.173
<i>STDE</i>	46.472	48.209	48.252	41.454	42.976	51.932	46.403	43.078	43.649	45.106	43.013	47.171	42.049

Table 5. Statistical metrics calculated for January 2019 hourly data at Barakah station.

	EXP01	EXP02	EXP03	EXP04	EXP05	EXP06	EXP07	EXP08	EXP09	EXP10	EXP11	EXP12	EXP13
2 m Air Temperature (°C)													
ρ	0.952	0.951	0.952	0.945	0.959	0.960	0.958	0.965	0.944	0.940	0.952	0.943	0.962
MB	0.138	0.488	0.680	0.444	0.501	-0.250	0.443	0.304	0.217	-0.120	0.836	0.977	0.179
MAE	1.050	1.140	1.193	1.247	1.042	0.942	1.084	0.949	1.202	1.211	1.315	1.475	1.003
RMSE	1.418	1.452	1.503	1.521	1.344	1.264	1.401	1.240	1.484	1.557	1.595	1.798	1.296
STDE	1.411	1.367	1.337	1.455	1.247	1.239	1.328	1.202	1.468	1.552	1.359	1.510	1.284
2 m Relative Humidity (%)													
ρ	0.896	0.890	0.901	0.908	0.904	0.883	0.901	0.919	0.906	0.893	0.907	0.902	0.913
MB	7.133	1.545	0.997	3.772	3.302	7.140	6.295	5.929	3.539	10.083	0.487	0.644	6.230
MAE	8.796	6.051	5.543	6.371	6.537	9.435	8.154	7.433	6.372	10.797	5.501	5.320	7.853
RMSE	11.201	8.486	7.775	8.757	8.470	11.441	10.418	9.498	8.637	13.207	7.595	7.538	10.014
STDE	8.636	8.344	7.711	7.903	7.801	8.940	8.302	7.419	7.879	8.530	7.579	7.510	7.840
10 m wind speed (m/s)													
ρ	0.840	0.822	0.829	0.823	0.831	0.823	0.839	0.867	0.815	0.819	0.823	0.822	0.863
MB	0.353	0.289	0.255	0.248	0.335	0.210	0.395	0.283	0.177	0.144	0.180	0.674	0.003
MAE	0.941	0.965	0.939	0.994	0.974	0.952	0.950	0.834	0.975	0.970	0.928	1.127	0.813
RMSE	1.254	1.309	1.268	1.318	1.292	1.292	1.269	1.135	1.326	1.305	1.274	1.439	1.117
STDE	1.203	1.277	1.243	1.294	1.248	1.275	1.206	1.099	1.314	1.297	1.261	1.271	1.117
10 m wind direction (°)													
ρ	0.862	0.863	0.868	0.879	0.886	0.841	0.867	0.894	0.880	0.876	0.891	0.850	0.896
MB	14.298	15.017	16.288	15.853	16.461	17.127	15.373	12.789	16.075	15.516	14.939	15.553	12.878
MAE	25.197	25.892	25.639	23.810	24.240	27.830	25.444	22.559	24.211	24.210	23.762	26.116	22.167
RMSE	39.332	40.075	40.480	36.092	36.415	42.514	39.745	36.067	36.090	36.097	37.143	39.670	36.129
STDE	36.641	37.155	37.058	32.424	32.483	38.912	36.651	33.724	32.313	32.593	34.006	36.494	33.756

Figure 7 displays mean diurnal variations for T2, and RH calculated for observations and the model simulations for January and June 2019. For June 2019, we note that all model simulations showed a noticeable consistent underprediction of the temperature, and the spread between the model simulations in the daytime is larger than during night-time and early morning. This underestimation indicates that the model has a systematic cold bias in this semi-arid region. This could probably be attributed to the higher cooling rate near the surface in the model compared to the observations which could be due to deficiencies in the physical parameterization schemes, in particular in the land surface model and radiation schemes, and/or a simplified representation of the atmospheric composition in the current WRF set up. Aerosol load and associated radiative impact [9] are known to exhibit an annual maximum during summer over the UAE [65]. This cold bias was also highlighted in the study carried out by Branch et al. [66] to assess the seasonal and daytime performance of daily forecasts with WRF in the United Arab Emirates. Note that the observed diurnal cycle was well simulated by EXP01, EXP08, and EXP13 than in the other model simulations, particularly during daytime.

However, for January 2019, we noted that the discrepancies between the different simulations are smaller compared to that of June 2019. All the simulations showed that the model tended to have a warm bias, but of less magnitude compared to that of June. This warm bias is probably due to an overestimation of downwelling surface shortwave in the WRF model, as previously highlighted in some studies over the UAE [62,65]. We noted the presence of a short reversal to a cold bias that occurred around 4 a.m. This switch usually occurred roughly around the twice-daily transition times of the boundary layer between stable and convective states [66].

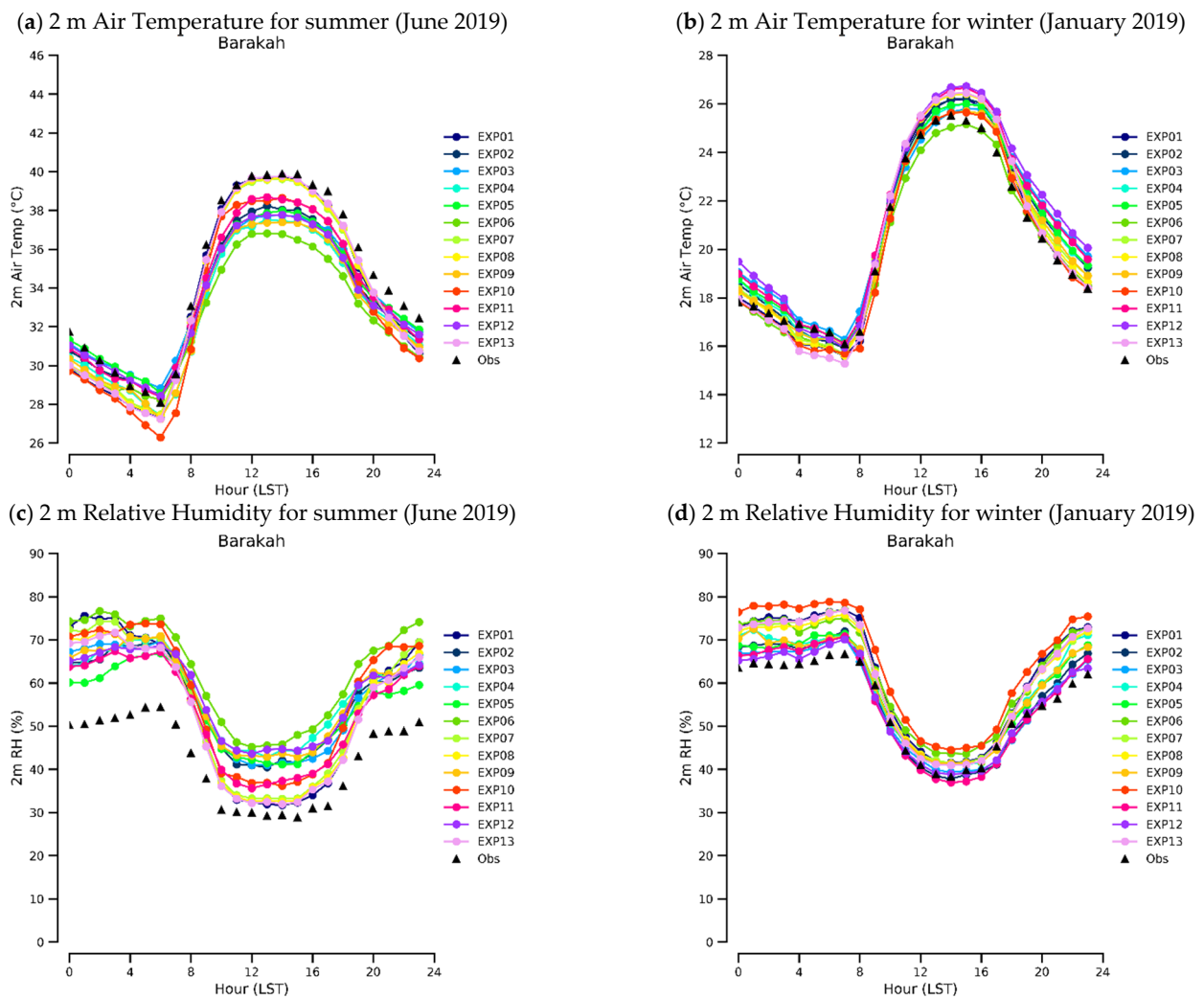


Figure 7. Mean diurnal variations for 2 m air temperature and relative humidity at Barakah station calculated for June and January 2019. The curve in black color shows the observation, while the others depict the different model simulations.

Regarding relative humidity, we note that for both January and June 2019, the observed diurnal cycle was overestimated (positive biases) by almost all the model simulations. This overestimation was more marked in June than in January. This could be attributed to the large cold bias in summer. The observed diurnal variation of RH is lower in June because this region is hot and dry during summer; however, most of the simulations could capture a similar trend of diurnal variation during both months. Notice that during January, exceptionally EXP11, and EXP12 showed a short shift in the sign of the bias occurred between 12 p.m. and 8 p.m. We also noticed that during the day, the observations were better reproduced by EXP08 and EXP13 in June, while in January, we note that the observations were well simulated by EXP11 and EXP12, instead.

3.4.2. Wind Speed and Direction

Statistical analysis of 10-m AGL wind speed (WS) and wind direction (WD) at Barakah station is presented in Tables 4 and 5. It is well known that surface wind speed and wind direction are significantly affected by local fluctuations particularly in highly unstable conditions [28]. However, the reported values indicate that the model using the different combinations of the physical options could reproduce the observed wind speed and direction with sufficient accuracy for June and January 2019. However, a general consistent overprediction in wind direction was observed in all simulations for both months. For June, we note that the model tended to underpredict the wind speed as indicated by the most of model configurations. Conversely, in January, all the model simulations indicated that the model had a general tendency to overpredict the wind speed. In addition, notice that

simulations EXP01, EXP08, and EXP13 performed better in terms of statistical evaluation than the other model experiments.

Figure 8 illustrates mean diurnal variations for WS and WD calculated for observations and the model using the different combinations of physical options for January and June 2019. Firstly, it can be noted that for both months, lower wind speeds were observed during the early morning and evening, while higher wind speeds occurred during the daytime. Lower and higher wind speeds are attributed to land and sea circulations, respectively. Note that the diurnal variation in the observations of WS and WD was more pronounced in June than in January. The spread between the model simulations for WS was also larger in June than in January, especially during the daytime. In general, we notice that the observed mean diurnal cycles of WS and WD were reasonably well reproduced by the model as observed in all the simulations. We note that EXP01, EXP08, and EXP13 were much closer to observations compared to the others. For January, we remark that the model showed a consistent overprediction of the WS. Inversely for June, we observed a shift from positive to negative bias that occurred around 9 a.m. This switch in the sign of the model bias is attributed to the change in the wind direction caused by sea and land breeze circulations. Specifically, the model overestimates wind speed with a magnitude of about 1 m s^{-1} in the morning and early morning hours and underestimates it in the afternoon and evening hours with a magnitude of about 1.5 m s^{-1} . The overproduction and underprediction of wind speed by the WRF model have been pointed out in many earlier studies [44,67–71].

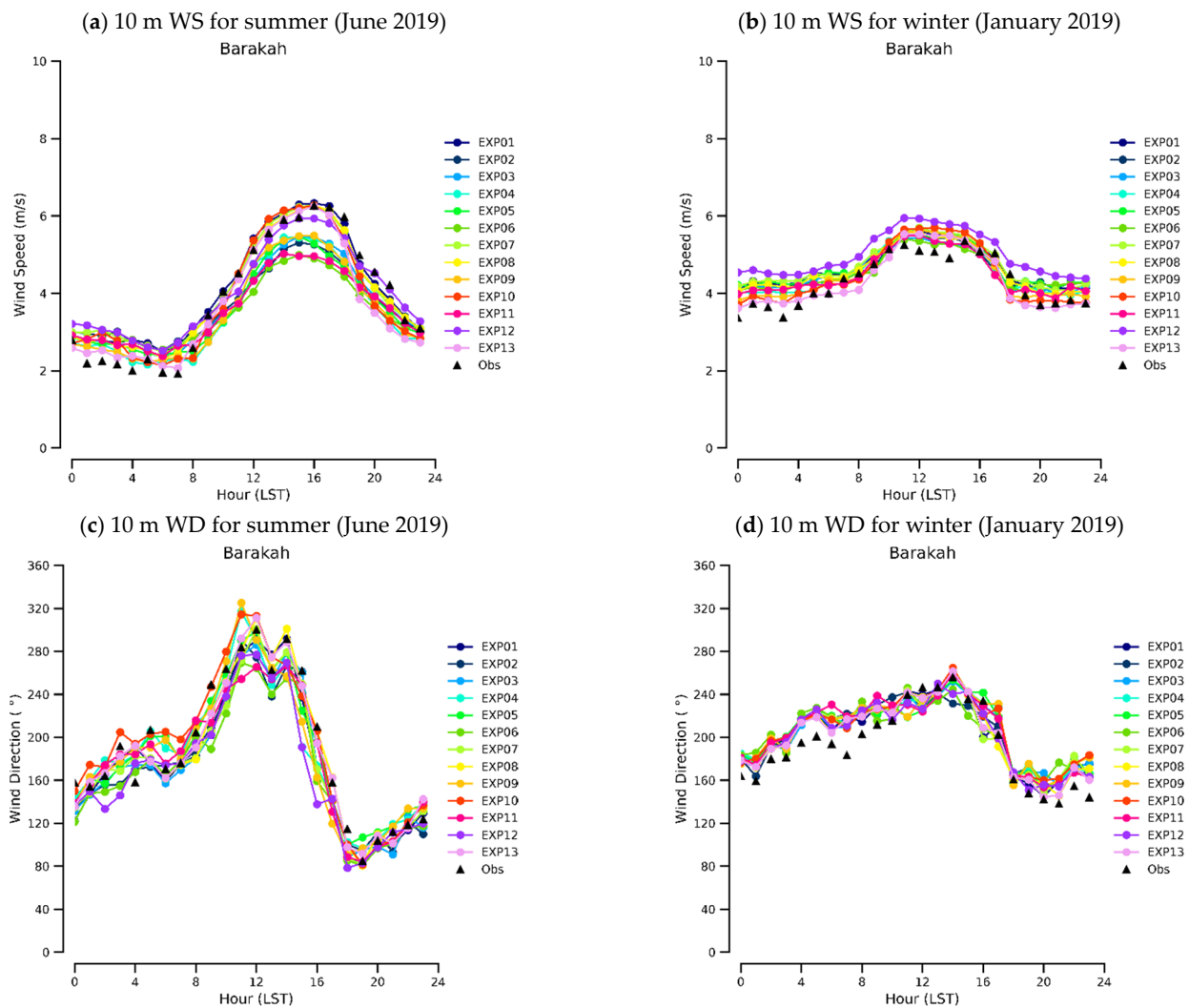


Figure 8. Mean diurnal variations for 10-m WS and WD at Barakah station calculated for June and January 2019. The curve in black color shows the observation, while the others depict the different model simulations.

In addition, the near-surface wind distribution is an important aspect to analyze to gain more insight into model wind simulation. To this end, using hourly data from the simulated and observed WS and WD, we calculated wind roses to represent the joint frequency distribution of WS and WD as well as wind speed histograms for June and January 1919.

Figures 9 and 10 depict the calculated wind roses for June and January respectively. The observed wind rose during June 2019, revealing that winds around BNPP blow mostly from northeast, north, and north-northeast. This is attributed to the sea breeze circulation which is very active during the summer and enhanced by large-scale weather patterns such as the Shamal winds. In June, we observe that all simulations showed similar patterns of wind direction but with relatively larger magnitudes compared to observations and could capture the main directions of the prevailing winds at Barakah station. Particularly, in the north direction, all simulations overestimated the wind speed frequency in 3–6 m s⁻¹. From wind roses, however, simulation EXP10, which contains the QNSE-EDMF scheme for PBL, was the closest to the observed pattern in terms of both direction and wind speed.

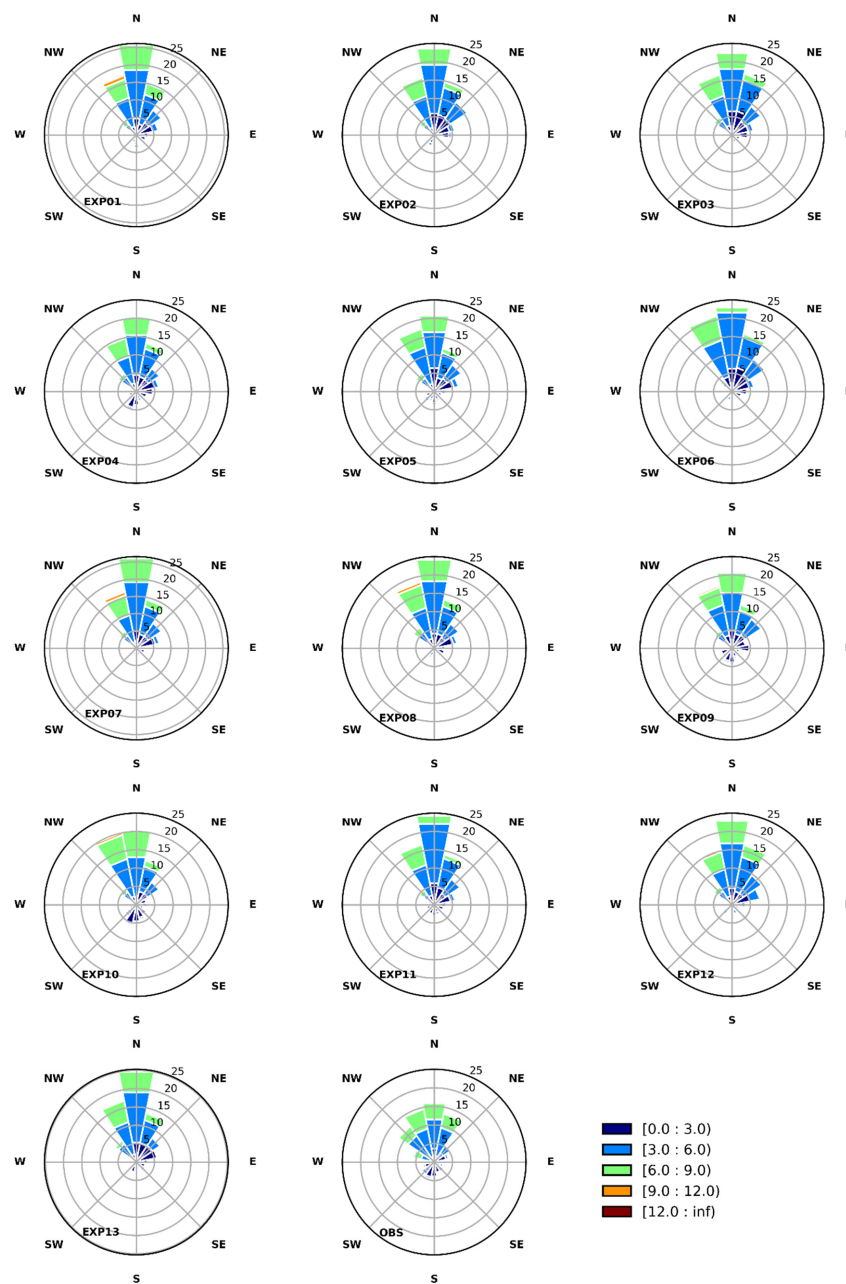


Figure 9. 10-m Wind roses at Barakah calculated for model simulations and observations for June 2019.

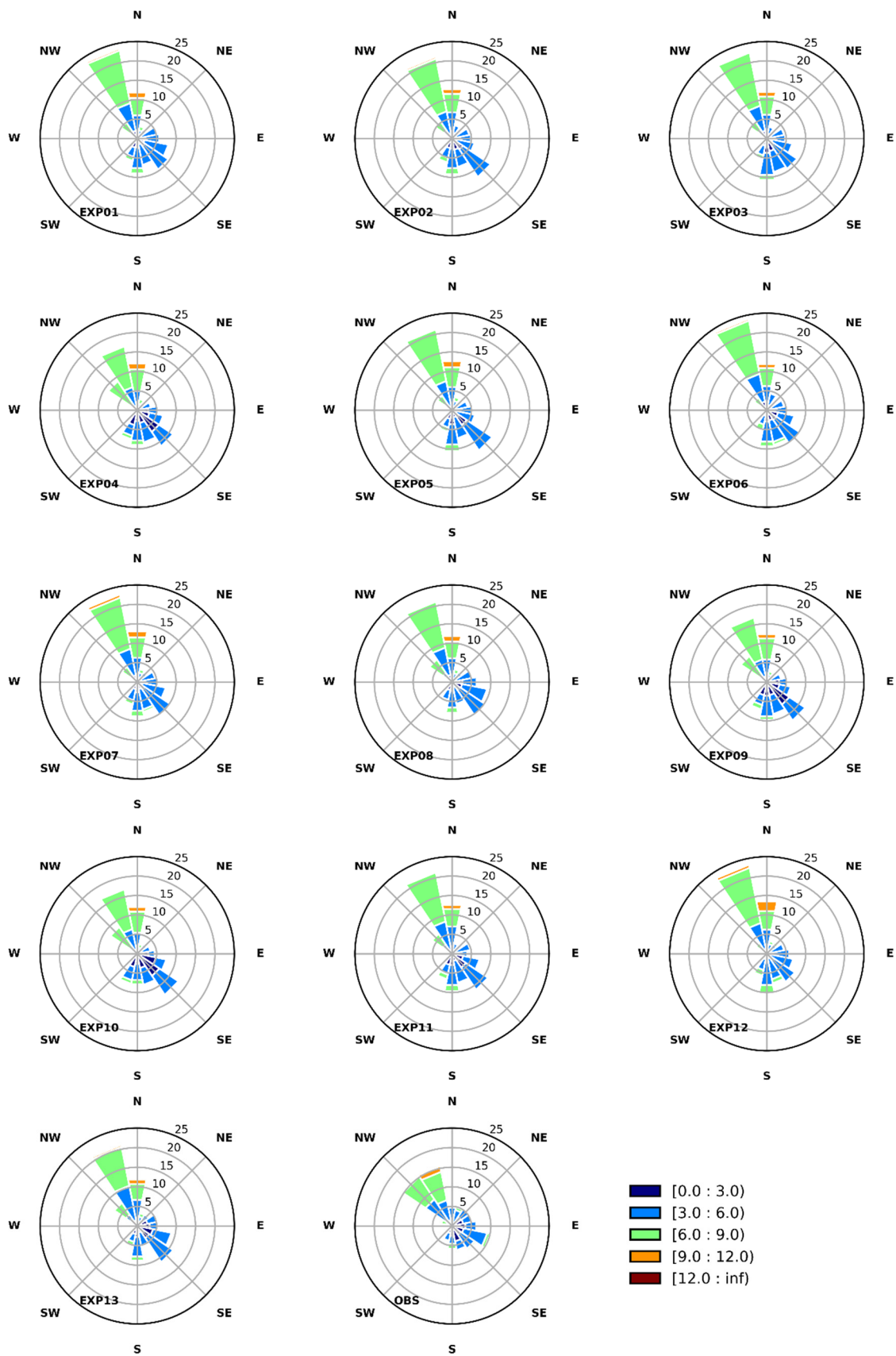


Figure 10. 10-m Wind roses at Barakah calculated for model simulations and observations for January 2019.

In January, the observed wind rose showed the prevailing winds were mostly from north, north-northeast, and southeast directions. The southeasterly winds are most likely generated by land breeze circulation. Similarly, we note that all the model experiments produced comparable wind direction patterns with relatively larger magnitudes compared to the observed wind rose. Note that, all the simulations are satisfactory for capturing the bimodal distribution of the wind observations reasonably well. In particular, we observe that the wind rose simulated from the EXP04 which also uses the QNSE-EDMF scheme for PBL, was the closest to the observed wind rose.

Figure 11 shows the calculated wind speed histograms for both January and June 2019. We note that all the simulated WS histograms are very comparable, and generally the observed distribution of WS was reasonably well reproduced by all the model simulations. Principally, we notice that the distribution of high wind speeds between 4 and 10 m s⁻¹ was better captured by the model as observed by all simulations compared to the distribution of low wind speeds (0–4 m s⁻¹). For both months, it can be seen that the model showed a tendency to overestimate and underestimate lower and higher winds respectively. We observe that the simulated histograms from EX10 and EXP04 were the closest to the observations for June and January, respectively.

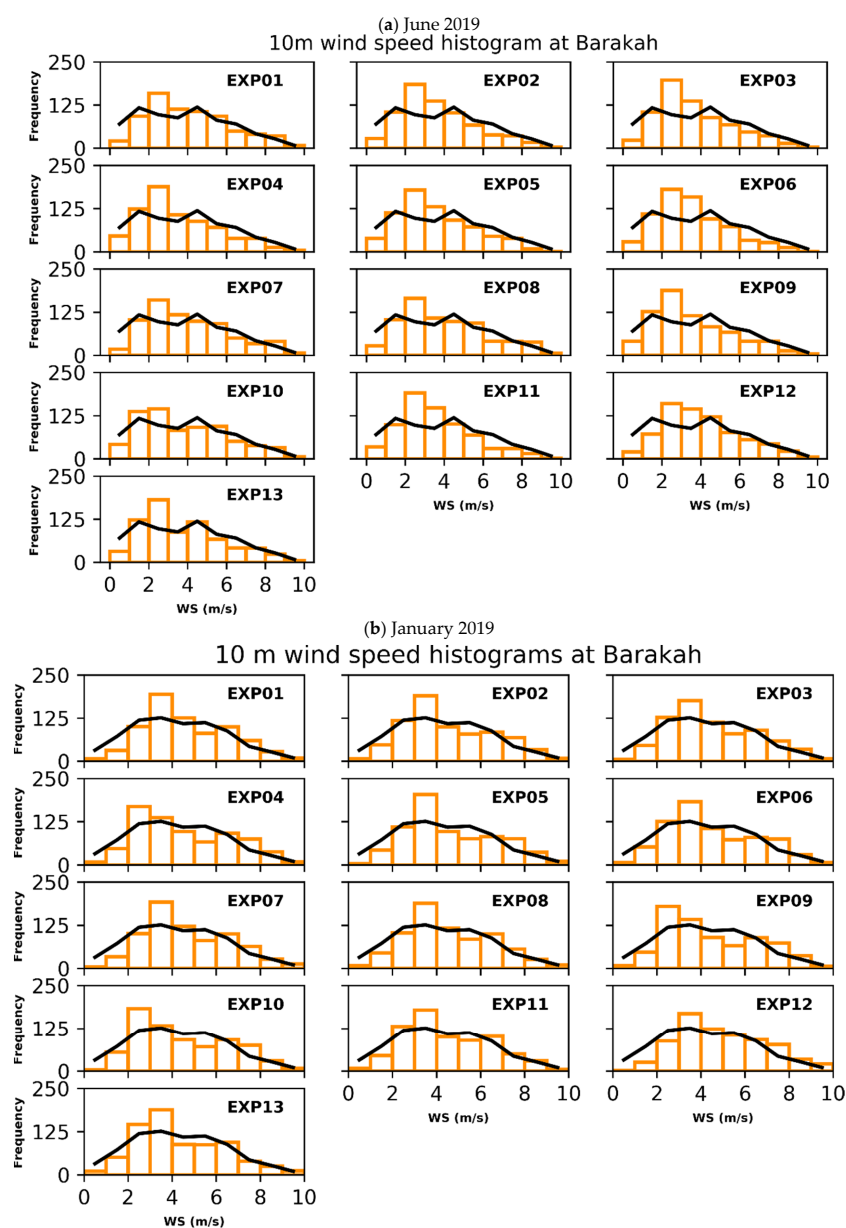


Figure 11. Histograms of simulated 10 m wind speed at Barakah for June (a) and January (b). The black line denotes the observed wind speed histogram. The orange lines depict the simulated histograms.

3.4.3. Model Simulations Ranking at Barakah

This section aims to rank the model simulations with respect to 2 m air temperature, relative humidity, and wind speed and direction at 10 m. However, it should be stressed that finding the optimal model options for a given parameter and season is application-dependent. For instance, the best performing options of temperature and relative humidity are relevant for fog studies, while the best performing options for wind velocity are preferred for dispersion applications. The relative rankings of different simulations can be changed if we look at different variables separately. One that performs in the simulation of 2 m air temperature might underperform for other thermodynamic variables. For example, EXP08 was found to better simulate 2 m air temperature but showed inferior outcomes for 2 m relative humidity.

To rank the various simulations, we combined statistical metrics calculated for the underlying surface parameters into Model Skill Scores (*MSSs*) as described in Section 2.4. Next, we averaged the calculated *MSS* values for the different variables. This way, each simulation was assigned a single scalar quantity. Hence, the simulation with the highest averaged *MSS* value (close to 5) was ranked as the best simulation and vice versa.

Figure 12 depicts the *MSS* calculated for each model simulation using hourly data during June and January 2019. *MSS* was calculated for morning and evening periods. Panels (a), (b) denote the *MSS* calculated with respect to the wind speed. While panels (c), and (d) show the averaged *MSS*. Panels (e), (f) depict the averaged *MSS* calculated for morning and evening periods. This figure shows a noticeable disparity in the relative ranking of the various simulations between summer and winter. The performance ranking of the simulations with respect to the wind speed—which is crucial for dispersion applications—shows that EXP08 and EXP13 constituted close to optimal combinations of model physics options. They had the highest *MSS* values among all other simulations for both June and January 2019. Specifically, we note that EXP08 performed better than EXP13 in June, while in January we observe the opposite. This result indicates that the topographic surface wind correction included in the EXP13 setting helps to better simulate the wind speed during winter. However, the relative ranking against all the variables again highlights that EXP08 and EXP13 still performed better than the other simulations for both June and January. These two simulations performed slightly better in summer.

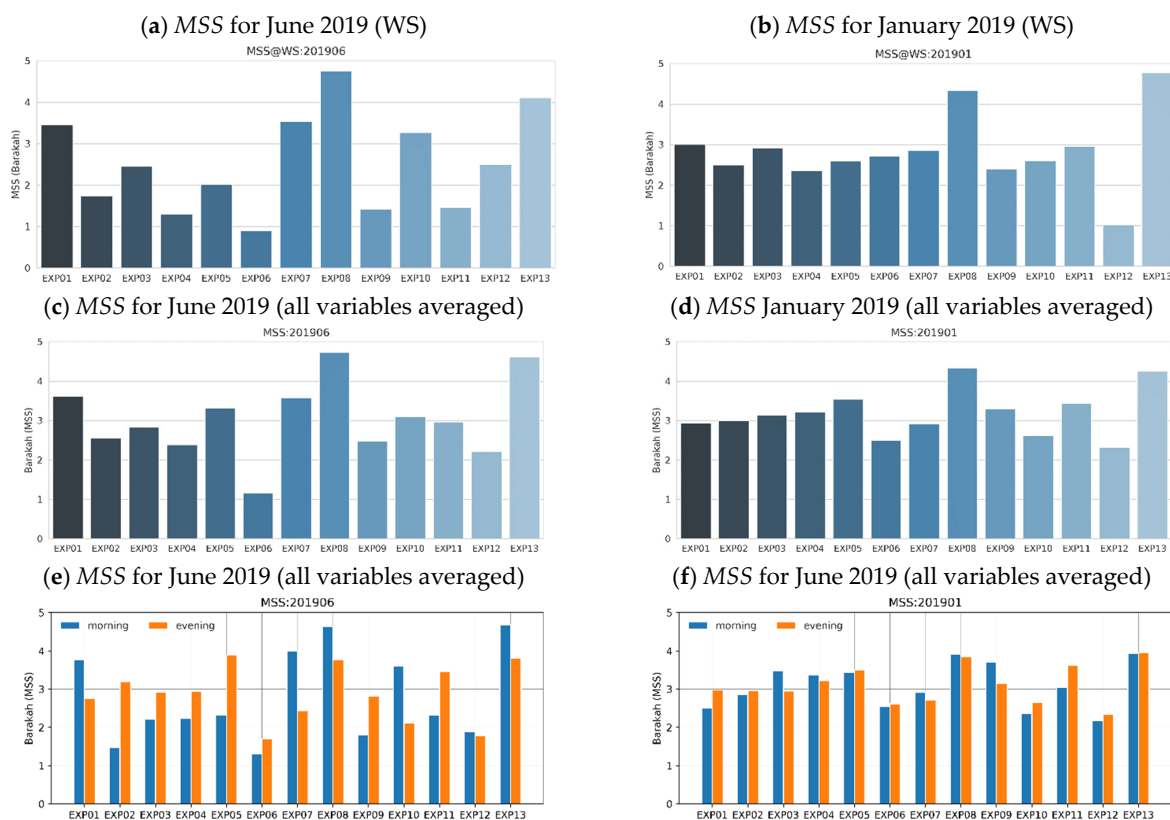


Figure 12. Model Skill Scores (*MSS*) at Barakah calculated for June and January 2019.

It is worth mentioning that the simulation EXP06, which contains the MYNN3 scheme for PBL and the Unified Noah Model for land surface, showed the lowest value of *MSS*, especially during summer. Therefore, this combination of model options is not appropriate for this coastal location. Panels (e), (f) show *MSS* values during morning and evening periods. Interestingly, during summer, we notice that optimal model simulations, EX08 and EXP13 performed better during the morning than in the evening. This indicates that the structure of the PBL is better simulated in the morning when it is more developed than in the evening. However, during winter, these two model experiments showed comparable performances during morning and evening periods.

3.5. Statistical Model Evaluation at a Downwind Site

This section aims to assess the performance of the model at a downwind location of BNPP. To this end, the statistical evaluation metrics were calculated for Aljazeera which is a downwind station located to the south of the nuclear site at 75 km.

Tables 6 and 7 summarize the calculated performance metrics for June and January 2019, respectively. It can be seen that the simulations EXP08 and EXP13 performed better compared to the others because they showed the lowest model errors and highest correlations for T2, RH, WS, and WD. However, for January, EXP11 proved to be more efficient for RH compared to the others. It is interesting to note that the calculated statistics for each model simulation were better than their corresponding statistics calculated for Barakah station. This result was already mentioned in Section 3.1, in that the model performed better inland compared to onshore or nearshore locations. For air temperature, we observe that all the simulations reported a negative mean bias (*MB*) with magnitudes in the range 0.4–1.7 °C in June. Inversely, during January most of the simulations showed a positive bias. This indicates that the WRF model in this semi-arid region tends to underestimate and overestimate air temperature in summer and winter, respectively. However, the model overestimated the relative humidity in both months, but with a larger magnitude in summer. Moreover, in both months, the model showed a tendency to underpredict the wind speed and overpredict the wind direction, as observed in all the simulations.

Table 6. Statistical metrics calculated for June 2019 hourly data at Aljazeera station.

	EXP01	EXP02	EXP03	EXP04	EXP05	EXP06	EXP07	EXP08	EXP09	EXP10	EXP11	EXP12	EXP13
2 m Air Temperature (K)													
<i>ρ</i>	0.986	0.982	0.985	0.977	0.977	0.977	0.986	0.990	0.978	0.980	0.980	0.981	0.992
<i>MB</i>	−0.785	−0.724	−0.703	−0.978	−0.567	−1.426	−0.739	−0.738	−0.981	−1.687	−0.443	−0.497	−0.643
<i>MAE</i>	1.129	1.116	1.037	1.355	1.147	1.604	1.039	0.957	1.337	1.845	1.040	1.104	0.863
<i>RMSE</i>	1.424	1.483	1.323	1.740	1.516	1.987	1.342	1.212	1.708	2.172	1.398	1.464	1.115
<i>STDE</i>	1.189	1.294	1.121	1.439	1.406	1.384	1.121	0.961	1.398	1.369	1.326	1.377	0.911
2 m Relative Humidity (%)													
<i>ρ</i>	0.946	0.943	0.938	0.928	0.934	0.922	0.944	0.956	0.936	0.920	0.939	0.936	0.961
<i>MB</i>	7.549	6.990	6.624	6.148	4.898	11.595	7.867	7.167	5.718	11.476	5.060	7.050	6.167
<i>MAE</i>	8.175	7.817	7.694	7.589	6.536	11.820	8.418	7.598	7.324	11.929	6.556	8.131	6.737
<i>RMSE</i>	11.423	11.026	10.666	10.945	9.681	15.644	11.456	10.266	10.522	15.216	9.611	11.317	9.297
<i>STDE</i>	8.573	8.527	8.360	9.055	8.351	10.502	8.329	7.350	8.833	9.991	8.171	8.853	6.956
10 m wind speed (m/s)													
<i>ρ</i>	0.89	0.887	0.888	0.858	0.877	0.885	0.890	0.918	0.859	0.864	0.890	0.875	0.914
<i>MB</i>	−0.408	−0.336	−0.429	−0.648	−0.553	−0.510	−0.458	−0.469	−0.560	−0.852	−0.420	0.058	−0.727
<i>MAE</i>	1.084	1.103	1.128	1.256	1.162	1.177	1.105	0.977	1.238	1.344	1.103	1.102	1.101
<i>RMSE</i>	1.426	1.439	1.469	1.673	1.551	1.534	1.449	1.290	1.634	1.735	1.438	1.461	1.427
<i>STDE</i>	1.366	1.401	1.405	1.542	1.449	1.446	1.374	1.202	1.535	1.511	1.376	1.460	1.228
10 m wind direction (°)													
<i>ρ</i>	0.715	0.707	0.726	0.698	0.757	0.707	0.711	0.787	0.685	0.662	0.724	0.687	0.799

Table 6. Cont.

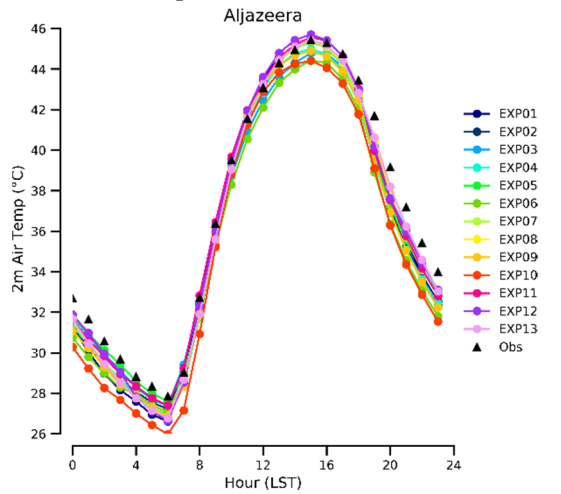
	EXP01	EXP02	EXP03	EXP04	EXP05	EXP06	EXP07	EXP08	EXP09	EXP10	EXP11	EXP12	EXP13
MB	12.528	13.661	11.115	9.316	10.763	12.385	12.741	10.266	8.971	9.181	11.716	13.459	8.492
MAE	25.759	26.374	26.231	25.998	24.109	26.999	25.499	22.068	26.306	26.774	24.981	27.048	20.942
RMSE	39.262	40.873	40.187	39.104	35.788	41.818	39.668	34.604	39.153	41.015	38.138	41.570	33.733
STDE	37.210	38.522	38.619	37.978	34.131	39.942	37.566	33.046	38.111	39.975	36.294	39.331	32.646

Table 7. Statistical metrics calculated for January 2019 hourly data at Aljazeera station.

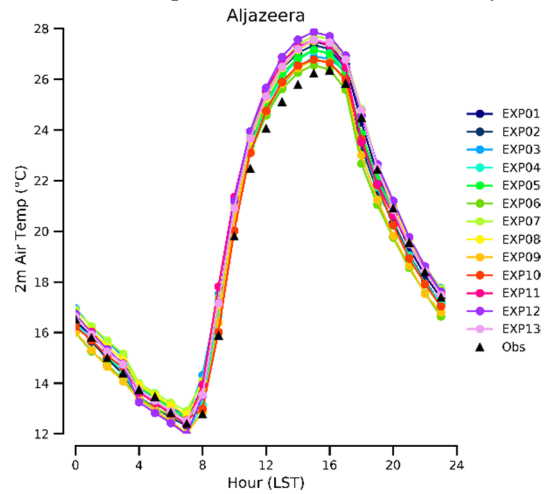
	EXP01	EXP02	EXP03	EXP04	EXP05	EXP06	EXP07	EXP08	EXP09	EXP10	EXP11	EXP12	EXP13
2 m Air Temperature (K)													
ρ	0.981	0.978	0.984	0.973	0.983	0.979	0.982	0.986	0.970	0.976	0.976	0.978	0.986
MB	0.482	0.263	0.433	0.117	0.417	−0.170	0.771	0.604	−0.183	0.032	0.525	0.606	0.543
MAE	0.947	0.968	0.887	1.091	0.890	0.920	1.082	0.901	1.101	0.978	1.112	1.151	0.892
RMSE	1.223	1.244	1.119	1.343	1.145	1.179	1.330	1.129	1.409	1.262	1.375	1.409	1.125
STDE	1.124	1.216	1.032	1.338	1.067	1.166	1.084	0.953	1.397	1.261	1.271	1.272	0.985
2 m Relative Humidity (%)													
ρ	0.915	0.924	0.929	0.920	0.921	0.893	0.920	0.935	0.923	0.913	0.927	0.926	0.935
MB	5.127	1.700	1.046	3.186	2.605	7.138	4.422	4.098	3.541	9.846	1.180	2.158	3.991
MAE	7.416	5.922	5.355	6.363	6.410	9.136	7.026	6.321	6.418	10.609	5.821	6.068	6.320
RMSE	10.221	8.193	7.629	8.898	8.631	12.429	9.651	8.703	8.802	13.115	7.893	8.581	8.601
STDE	8.842	8.014	7.557	8.308	8.228	10.176	8.579	7.677	8.058	8.663	7.804	8.305	7.618
10 m wind speed (m/s)													
ρ	0.841	0.868	0.857	0.845	0.876	0.854	0.853	0.885	0.845	0.844	0.870	0.853	0.886
MB	−0.090	−0.045	−0.032	−0.291	−0.155	−0.054	−0.026	−0.092	−0.338	−0.438	−0.086	0.377	−0.332
MAE	0.878	0.891	0.867	0.879	0.818	0.944	0.853	0.768	0.891	0.913	0.832	0.960	0.801
RMSE	1.242	1.161	1.200	1.260	1.125	1.215	1.196	1.080	1.271	1.302	1.151	1.253	1.133
STDE	1.239	1.160	1.200	1.226	1.114	1.214	1.196	1.076	1.225	1.226	1.148	1.195	1.083
10 m wind direction (°)													
ρ	0.871	0.870	0.867	0.833	0.864	0.878	0.875	0.906	0.837	0.847	0.865	0.846	0.915
MB	13.465	13.323	12.718	8.788	11.687	15.240	13.305	11.929	7.900	8.980	11.983	14.440	10.784
MAE	21.983	22.759	23.041	23.013	22.087	23.335	22.079	19.218	23.329	22.023	22.068	23.988	18.370
RMSE	32.489	33.940	34.995	37.305	34.217	32.511	32.595	28.930	37.167	35.095	34.573	35.415	28.104
STDE	29.568	31.216	32.602	36.255	32.159	28.718	29.756	26.356	36.318	33.927	32.430	32.337	25.952

Figure 13 depicts mean diurnal variations for T2, RH, and WS calculated at the Aljazeera location for June and January 2019. For air temperature, the observed diurnal cycle was globally well reproduced by the model within a range of error less than ± 2 °C for both months. Specifically, we remark that the model showed consistent cold and warm biases in June and January respectively. Notice that spread between the various simulations is smaller compared to that of Barakah. For relative humidity, we note the values of the observed diurnal cycle were higher in January than in June. Generally, it can be noted that for both months, the model had an overall consistent positive bias as observed in most simulations. This systematic bias was particularly more pronounced in the early morning and evening. Yet, in January, we observe that some model simulations for example EXP11, EXP12 showed a switch from positive biases in the early morning and evening to negative biases in the daytime but with lower magnitudes.

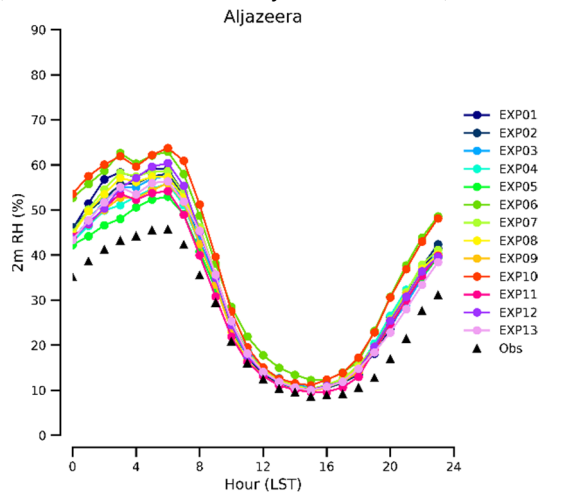
(a) 2 m Air Temperature for summer (June 2019)



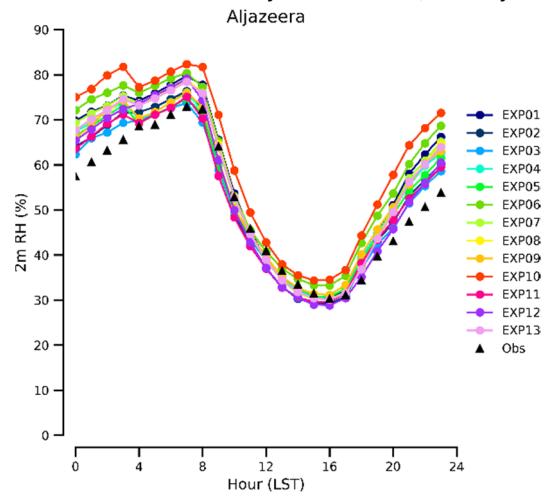
(b) 2 m Air Temperature for winter (January 2019)



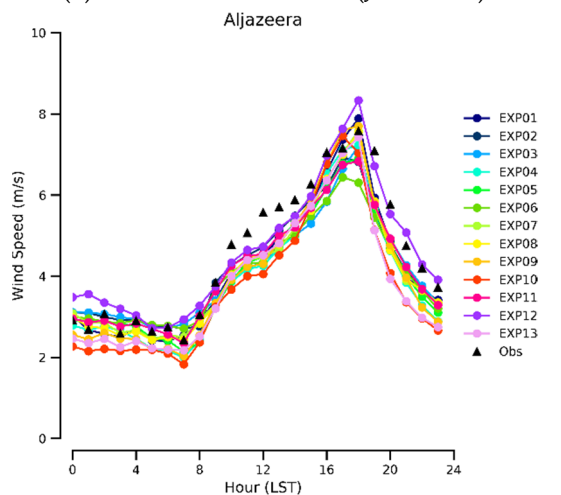
(c) 2 m Relative Humidity for summer (June 2019)



(d) 2 m Relative Humidity for winter (January 2019)



(e) 10 m WS for summer (June 2019)



(f) 10 m WS for winter (January 2019)

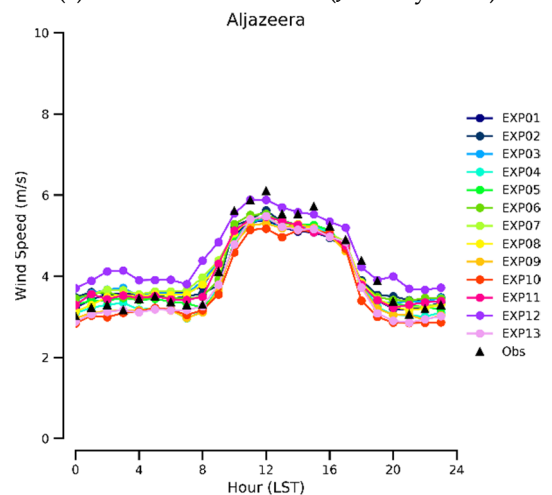


Figure 13. Mean diurnal variations for T2, RH, and WS calculated at Aljazeera station calculated for June and January 2019. The curve in black color shows the observation, while the others depict the different model simulations.

Regarding wind speed, we note that the diurnal variations in the observations were reasonably well captured by all the model simulations with errors of less than 2 m s^{-1} . However, also note that

most simulations underpredicted the observed diurnal cycle with different magnitudes. This indicates that the model tends to underestimate the wind speed at that inland location, particularly during summer. In addition, note that the amplitudes of the observed and simulated diurnal variations were greater at this location than at Barakah. Interestingly, note that in both months, the EXP12 simulation, in terms of average bias was closest to the observed diurnal cycle. EXP12 used the YSU scheme for PBL, the Noah-MP model for the land surface, and the revised MM5 for the surface layer scheme.

Additionally, to investigate how the model performed in terms of simulating the wind distribution at Aljazeera station, we calculated wind roses at that location to represent the joint frequency distribution of WS and WD as well as wind speed histograms for June and January 2019. Figure 14 depicts the simulated and observed wind distribution at Aljazeera site. The wind roses calculated for the different simulations showed very similar wind distribution patterns, and the same is true for the simulated histograms. Therefore, we only show the simulated wind roses and wind speed histograms of EXP13, which showed better performance in terms of model errors (see Tables 6 and 7). In June, the observed wind rose indicates that winds at al Jazeera are mostly from north-northeast, north, and north-northwest. This pattern in wind directions is most likely associated with the active sea breeze circulation during summer

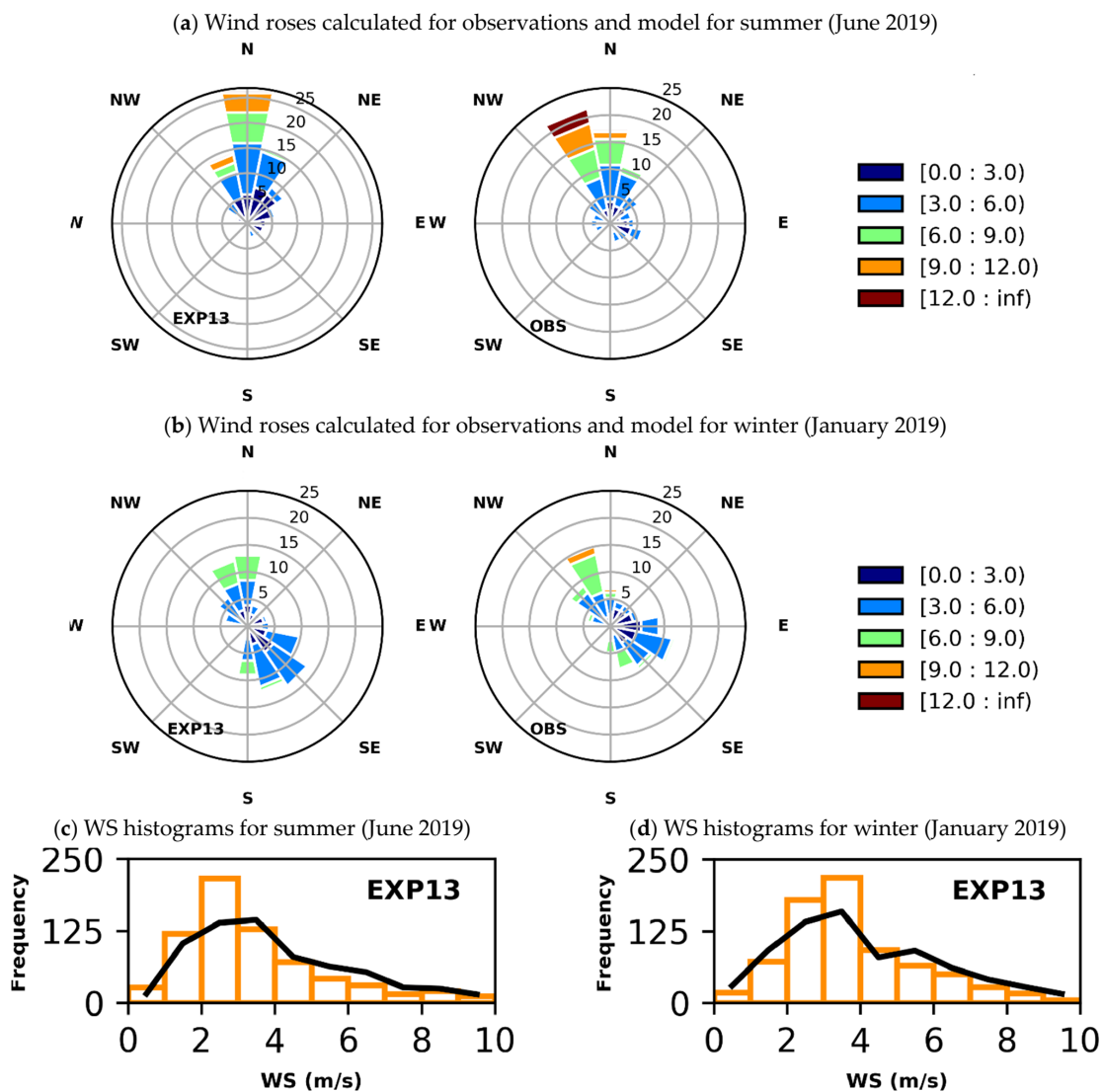


Figure 14. 10-m wind roses and wind speed histograms calculated for model and observations at Aljazeera for June and January 2019. (a,b) denote the observed and the simulated wind roses for June and January respectively. (c,d) show respectively the observed (black curve) and the simulated (orange curve) histograms for June and January 2019.

We notice that the model captured the main prevailing wind directions but mostly overestimated the frequency of the wind direction. In January, the wind rose of the observations showed that winds were mainly blowing from north-northwest, northwest, and east-southeast. This wind direction distribution at Aljazeera is principally attributed to the transition between sea breeze and land breeze in the course of the day during the winter season. Note that the model reproduced the bimodal wind distribution reasonably well in the observations. However, the model tended to overestimate the frequency of wind speed especially in the range 3–6 m s⁻¹. Additionally, the wind speed histograms for both months, show that the model could simulate with sufficient accuracy the high wind speed distribution (4–10 m s⁻¹). However, we observe that the model generally tended to overestimate the frequency of the low wind speeds (0–4 m s⁻¹).

Model Simulations Ranking at Aljazeera

In this section, we present the results related to the statistical ranking of the various model simulations at Aljazeera. Figure 15 shows the relative ranking calculated for June and January 2019. Panels (a), and (b) show the relative ranking with respect to the wind speed, while (c) and (d) depict the relative ranking considering all the surface variables: T2, RH, WS, and WD. Globally we notice more variability in Model Skill Score (MSS) values, especially during June. The ranking against wind speed shows that EXP08 outperformed other simulations in June, whereas in January we notice that EXP13 worked better instead. However, the relative ranking against all the variables, shows that EXP08 and EXP13 outperformed the other simulations in both months. In June, EXP13 behaved slightly better than EXP08 while the opposite was observed in January. In addition, the averaged MSS calculated during the morning and the evening periods highlights that globally, the model performance was better in the morning than in the evening periods.

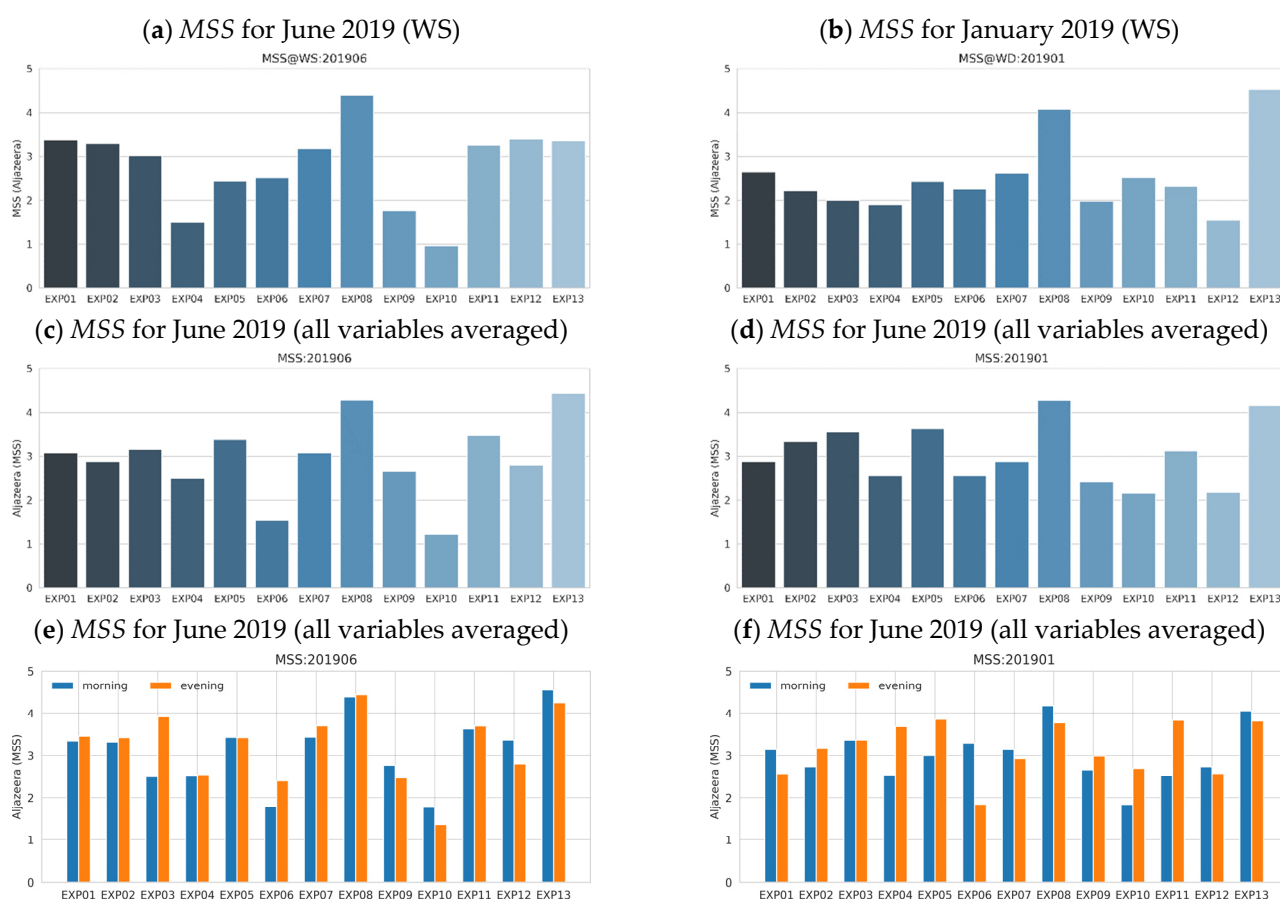


Figure 15. Model Skill Score (MSS) at Aljazeera calculated for June and January 2019.

4. Summary and Conclusions

A sensitivity study was conducted using the WRF model to investigate which of the available physics options generate the most accurate results for surface meteorological variables in a coastal

hyper-arid region in the western desert of the UAE. This specific region is of great importance as it hosts the BNPP. This makes it paramount to correctly simulate local weather conditions in this region for emergency response in case of an atmospheric accidental radioactive release occurring at BNPP.

In this regard, a series of high-resolution model simulations using different combinations of physical schemes were conducted over January and June 2019 over the targeted region.

The simulated results were verified against the in situ meteorological surface measurements available within a radius of 150 km around the nuclear site. Several statistical metrics were calculated to quantify the impact of the various model runs on the modeled results and then find a near-optimal set of physics options that optimize the WRF model over this region and particularly at the BNPP location.

The overall performance of the WRF model was assessed at different locations around BNPP. The first results revealed a gradual transition in the performance of the model when moving from sea to land. Explicitly, it was found that the model performed better at inland locations than at sea locations. This sea-to-land transition in model performance was found to be essentially more pronounced in 2 m air temperature and relative humidity. These results also ascertain that the performance of non-hydrostatic short-scale simulations is highly region-dependent and that no single set of physical options can be designated as an optimal model setup for all the locations in the studied region. Yet, globally, it was found that WSM 3-class microphysics, RRTM for longwave radiation, RTTMG for shortwave radiation, Kain-Fritsch cumulus, revised MM5 Monin-Obukhov surface layer, thermal diffusion scheme, and YSU PBL combination generated better results at most locations compared to other sets of physical options.

In addition to the sensitivity to physics options, we also investigated the impact of two dynamics options on the model performance: surface station nudging and horizontal model resolution. It was found that the station nudging has the potential to alleviate the model imbalance by extracting mesoscale information from surface stations and subsequently reducing the model error. Particularly, the nudging results showed an overall reduction in model errors, which was more marked at onshore and nearshore locations. Moreover, it was found that the higher horizontal resolution had a clear benefit on the model performance. Specifically, statistics calculated with a spatial resolution of 1 km, were significantly better than those calculated with a spatial resolution of 5 or 25 km. This result indicates that the mesoscale coastal circulation is better resolved in high-resolution simulation than at coarse spatial resolution. In addition, it was noticed that the benefit of high spatial resolution was particularly more pronounced at onshore and nearshore sites compared to inland sites.

Additionally, the relative rankings of the various sensitivity simulations were calculated by combining all the statistical performance indicators into Model Skill Scores. The relative ranking obtained by considering all surface variables was presented for Barakah and Al Jazeera stations. The results indicate that globally the following physics options: WSM 3-class microphysics, RRTM for longwave radiation, RTTMG for shortwave radiation, Kain-Fritsch cumulus, revised MM5 Monin-Obukhov surface layer, thermal diffusion scheme, and YSU PBL constitute a near to optimal combination of physical parameterization schemes that optimizes the WRF model at these two locations during summer and winter periods. However, the ranking of the different simulations with respect to the wind speed parameter revealed that adding the topographic correction option for surface winds to the previous physical options had a positive impact on wind speed simulation, especially in winter. It was also found that the WRF model performed better in the morning than in the evening periods.

This study will be extended to include surface radiative fluxes and upper air meteorological measurements at BNPP. We aim to use the best-performing combination of physical options found in this study as the basis for a new series of sensitivity tests in which additional sets of physical options will be explored.

Author Contributions: Conceptualization, R.A. and Y.A.; methodology, R.A. and Y.A.; software, R.A.; validation, R.A.; writing—original draft preparation, R.A.; writing—review and editing, R.A., Y.A., M.T., O.N., N.N., R.F. and E.B.; methodology: R.A., Y.A., D.F.; funding acquisition: E.B. All authors have read and agreed to the published version of the manuscript.

Funding: This research and the APC were funded by the Federal Authority for Nuclear Regulation in the UAE through the MORAD research project.

Data Availability Statement: Model simulations are hosted at: <https://kudrive.ku.ac.ae/oc-shib/index.php/s/yqsypEOTnBV5Fnk>, accessed on 15 May 2022. Access to observation data requires a case-by-case approval from the owner.

Acknowledgments: The authors would like to thank Khalifa University’s high-performance computing and research computing facilities for their support of this research work. The Federal Authority for Nuclear Regulation (FANR) in the UAE is acknowledged for funding the MORAD research project aiming to study atmospheric and marine radionuclide dispersion over the United Arab Emirates. The National Center of the Meteorology (NCM) is acknowledged for sharing ground-based station data. We would like to thank Nawah for hosting meteorological instruments and sharing their weather tower data.

Conflicts of Interest: The authors declare no conflict of interest.

References

1. Nesterov, O.; Temimi, M.; Fonseca, R.; Nelli, N.R.; Addad, Y.; Bosc, E.; Abida, R. Validation and Statistical Analysis of the Group for High Resolution Sea Surface Temperature Data in the Arabian Gulf. *Oceanologia* **2021**, *63*, 497–515. [[CrossRef](#)]
2. Lelieveld, J.; Proestos, Y.; Hadjinicolaou, P.; Tanarhte, M.; Tyrlis, E.; Zittis, G. Strongly Increasing Heat Extremes in the Middle East and North Africa (MENA) in the 21st Century. *Clim. Chang.* **2016**, *137*, 245–260. [[CrossRef](#)]
3. Feng, S.; Hu, Q.; Huang, W.; Ho, C.-H.; Li, R.; Tang, Z. Projected Climate Regime Shift under Future Global Warming from Multi-Model, Multi-Scenario CMIP5 Simulations. *Glob. Planet. Chang.* **2014**, *112*, 41–52. [[CrossRef](#)]
4. Nelli, N.R.; Temimi, M.; Fonseca, R.M.; Weston, M.J.; Thota, M.S.; Valappil, V.K.; Branch, O.; Wizemann, H.D.; Wulfmeyer, V.; Wehbe, Y. Micrometeorological Measurements in an Arid Environment: Diurnal Characteristics and Surface Energy Balance Closure. *Atmos. Res.* **2020**, *234*, 104745. [[CrossRef](#)]
5. Böer, B. An Introduction to the Climate of the United Arab Emirates. *J. Arid Environ.* **1997**, *35*, 3–16. [[CrossRef](#)]
6. Francis, D.; Temimi, M.; Fonseca, R.; Nelli, N.R.; Abida, R.; Weston, M.; Whebe, Y. On the Analysis of a Summertime Convective Event in a Hyperarid Environment. *Q. J. R. Meteorol. Soc.* **2021**, *147*, 501–525. [[CrossRef](#)]
7. Weston, M.J.; Temimi, M.; Burger, R.P.; Piketh, S.J. A Fog Climatology at Abu Dhabi International Airport. *J. Appl. Meteorol. Climatol.* **2021**, *60*, 223–236. [[CrossRef](#)]
8. Weston, M.; Francis, D.; Nelli, N.; Fonseca, R.; Temimi, M.; Addad, Y. The First Characterisation of Fog Microphysics in the United Arab Emirates, an Arid Region on the Arabian Peninsula. *Earth Space Sci.* **2022**, *9*, 2021EA002032. [[CrossRef](#)]
9. Fonseca, R.; Francis, D.; Weston, M.; Nelli, N.; Farah, S.; Wehbe, Y.; AlHosari, T.; Teixido, O.; Mohamed, R. Sensitivity of Summertime Convection to Aerosol Loading and Properties in the United Arab Emirates. *Atmosphere* **2021**, *12*, 1687. [[CrossRef](#)]
10. Francis, D.; Chaboureau, J.-P.; Nelli, N.; Cuesta, J.; Alshamsi, N.; Temimi, M.; Pauluis, O.; Xue, L. Summertime Dust Storms over the Arabian Peninsula and Impacts on Radiation, Circulation, Cloud Development and Rain. *Atmos. Res.* **2021**, *250*, 105364. [[CrossRef](#)]
11. Al Jallad, F.; Al Katheeri, E.; Al Omar, M. Levels of Particulate Matter in Western UAE Desert and Factors Affecting Their Distribution. *Artif. Intell. Rev.* **2013**, *174*, 111–122. [[CrossRef](#)]
12. Abida, R.; Bocquet, M. Targeting of Observations for Accidental Atmospheric Release Monitoring. *Atmos. Environ.* **2009**, *43*, 6312–6327. [[CrossRef](#)]
13. Abida, R.; Bocquet, M.; Vercauteren, N.; Isnard, O. Design of a Monitoring Network over France in Case of a Radiological Accidental Release. *Atmos. Environ.* **2008**, *42*, 5205–5219. [[CrossRef](#)]
14. Korsakissok, I.; Mathieu, A.; Didier, D. Atmospheric Dispersion and Ground Deposition Induced by the Fukushima Nuclear Power Plant Accident: A Local-Scale Simulation and Sensitivity Study. *Atmos. Environ.* **2013**, *70*, 267–279. [[CrossRef](#)]
15. Yoshikane, T.; Yoshimura, K. Dispersion Characteristics of Radioactive Materials Estimated by Wind Patterns. *Sci. Rep.* **2018**, *8*, 9926. [[CrossRef](#)]
16. Yoshikane, T.; Yoshimura, K.; Chang, E.-C.; Saya, A.; Oki, T. Long-Distance Transport of Radioactive Plume by Nocturnal Local Winds. *Sci. Rep.* **2016**, *6*, 36584. [[CrossRef](#)]
17. Aird, J.A.; Barthelmie, R.J.; Shepherd, T.J.; Pryor, S.C. WRF-Simulated Low-Level Jets over Iowa: Characterization and Sensitivity Studies. *Wind Energy Sci.* **2021**, *6*, 1015–1030. [[CrossRef](#)]
18. Chaouch, N.; Temimi, M.; Weston, M.; Ghedira, H. Sensitivity of the Meteorological Model WRF-ARW to Planetary Boundary Layer Schemes during Fog Conditions in a Coastal Arid Region. *Atmos. Res.* **2017**, *187*, 106–127. [[CrossRef](#)]
19. Fu, G.; Guo, J.; Xie, S.; Duan, Y.; Zhang, M. Analysis and High-Resolution Modeling of a Dense Sea Fog Event over the Yellow Sea. *Atmos. Res.* **2006**, *81*, 293–303. [[CrossRef](#)]
20. Gao, S.; Lin, H.; Shen, B.; Fu, G. A Heavy Sea Fog Event over the Yellow Sea in March 2005: Analysis and Numerical Modeling. *Adv. Atmos. Sci.* **2007**, *24*, 65–81. [[CrossRef](#)]
21. Hernández-Ceballos, M.A.; Adame, J.A.; Bolívar, J.P.; de la Morena, B.A. A Mesoscale Simulation of Coastal Circulation in the Guadalquivir Valley (Southwestern Iberian Peninsula) Using the WRF-ARW Model. *Atmos. Res.* **2013**, *124*, 1–20. [[CrossRef](#)]
22. Steele, C.J.; Dorling, S.R.; von Glasow, R.; Bacon, J. Idealized WRF Model Sensitivity Simulations of Sea Breeze Types and Their Effects on Offshore Windfields. *Atmos. Chem. Phys.* **2013**, *13*, 443–461. [[CrossRef](#)]
23. Tay, K.; Koh, T.-Y.; Skote, M. Characterizing Mesoscale Variability in Low-Level Jet Simulations for CBLAST-LOW 2001 Campaign. *Meteorol. Atmos. Phys.* **2021**, *133*, 163–179. [[CrossRef](#)]

24. Yang, Y.; Hu, X.; Gao, S.; Wang, Y. Sensitivity of WRF Simulations with the YSU PBL Scheme to the Lowest Model Level Height for a Sea Fog Event over the Yellow Sea. *Atmos. Res.* **2019**, *215*, 253–267. [[CrossRef](#)]
25. Powers, J.G.; Klemp, J.B.; Skamarock, W.C.; Davis, C.A.; Dudhia, J.; Gill, D.O.; Coen, J.L.; Gochis, D.J.; Ahmadov, R.; Peckham, S.E.; et al. The Weather Research and Forecasting Model: Overview, System Efforts, and Future Directions. *Bull. Am. Meteorol. Soc.* **2017**, *98*, 1717–1737. [[CrossRef](#)]
26. Leelőssy, Á.; Molnár, F.; Izsák, F.; Havasi, Á.; Lagzi, I.; Mészáros, R. Dispersion Modeling of Air Pollutants in the Atmosphere: A Review. *Cent. Eur. J. Geosci.* **2014**, *6*, 257–278. [[CrossRef](#)]
27. Storm, B.A.; Dudhia, J.; Basu, S.; Swift, A.J.; Giammanco, I.M. Evaluation of the Weather Research and Forecasting Model on Forecasting Low level Jets: Implications for Wind Energy. *Wind Energy* **2009**, *12*, 81–90. [[CrossRef](#)]
28. Hu, X.; Nielsen-Gammon, J.W.; Zhang, F. Evaluation of Three Planetary Boundary Layer Schemes in the WRF Model. *J. Appl. Meteorol. Climatol.* **2010**, *49*, 1831–1844. [[CrossRef](#)]
29. Kleczek, M.A.; Steeneveld, G.-J.; Holtslag, A.A.M. Evaluation of the Weather Research and Forecasting Mesoscale Model for GABL53: Impact of Boundary-Layer Schemes, Boundary Conditions and Spin-Up. *Bound. Layer Meteorol.* **2014**, *152*, 213–243. [[CrossRef](#)]
30. Rajeevan, M.; Kesarkar, A.P.; Thampi, S.B.; Rao, T.N.; Radhakrishna, B.P.; Rajasekhar, M. Sensitivity of WRF Cloud Microphysics to Simulations of a Severe Thunderstorm Event over Southeast India. *Ann. Geophys.* **2010**, *28*, 603–619. [[CrossRef](#)]
31. Floors, R.; Vincent, C.L.; Gryning, S.-E.; Peña, A.; Batchvarova, E. The Wind Profile in the Coastal Boundary Layer: Wind Lidar Measurements and Numerical Modelling. *Bound. Layer Meteorol.* **2013**, *147*, 469–491. [[CrossRef](#)]
32. Yang, Q.; Berg, L.K.; Pekour, M.S.; Fast, J.D.; Newsom, R.; Stoelinga, M.T.; Finley, C.A. Evaluation of WRF-Predicted Near-Hub-Height Winds and Ramp Events over a Pacific Northwest Site with Complex Terrain. *J. Appl. Meteorol. Climatol.* **2013**, *52*, 1753–1763. [[CrossRef](#)]
33. Soni, M.; Payra, S.; Sinha, P.; Verma, S. A Performance Evaluation of WRF Model Using Different Physical Parameterization Scheme during Winter Season over a Semi-Arid Region, India. *Inter. J. Earth Atmos. Sci.* **2014**, *1*, 104–114.
34. Carvalho, D.; Rocha, A.; Gómez-Gesteira, M.; Santos, C. A Sensitivity Study of the WRF Model in Wind Simulation for an Area of High Wind Energy. *Environ. Model. Softw.* **2012**, *33*, 23–34. [[CrossRef](#)]
35. Dzebre, D.E.; Acheampong, A.A.; Ampofo, J.; Adaramola, M.S. A Sensitivity Study of Surface Wind Simulations over Coastal Ghana to Selected Time Control and Nudging Options in the Weather Research and Forecasting Model. *Heliyon* **2019**, *5*, e01385. [[CrossRef](#)]
36. Chadee, X.T.; Seegobin, N.R.; Clarke, R.M. Optimizing the Weather Research and Forecasting (WRF) Model for Mapping the Near-Surface Wind Resources over the Southernmost Caribbean Islands of Trinidad and Tobago. *Energies* **2017**, *10*, 931. [[CrossRef](#)]
37. Tyagi, B.; Magliulo, V.; Finardi, S.; Gasbarra, D.; Carlucci, P.; Toscano, P.; Zaldei, A.; Riccio, A.; Calori, G.; D’Allura, A.; et al. Performance Analysis of Planetary Boundary Layer Parameterization Schemes in WRF Modeling Set Up over Southern Italy. *Atmosphere* **2018**, *9*, 272. [[CrossRef](#)]
38. Boadh, R.; Satyanarayana, A.N.V.; Rama Krishna, T.V.B.P.S.; Madala, S. Sensitivity of PBL Schemes of the WRF-ARW Model in Simulating the Boundary Layer Flow Parameters for Their Application to Air Pollution Dispersion Modeling over a Tropical Station. *Atmósfera* **2016**, *29*, 61–81. [[CrossRef](#)]
39. Taraphdar, S.; Pauluis, O.M.; Xue, L.; Liu, C.; Rasmussen, R.; Ajayamohan, R.S.; Tessendorf, S.; Jing, X.; Chen, S.; Grabowski, W.W. WRF Gray-Zone Simulations of Precipitation Over the Middle-East and the UAE: Impacts of Physical Parameterizations and Resolution. *J. Geophys. Res. Atmos.* **2021**, *126*, e2021JD034648. [[CrossRef](#)]
40. Yu, N.; Barthe, C.; Plu, M. Evaluating Intense Precipitation in High-Resolution Numerical Model over a Tropical Island: Impact of Model Horizontal Resolution. *Nat. Hazards Earth Syst. Sci. Discuss* **2014**, *2*, 999–1032. [[CrossRef](#)]
41. Pokhrel, R.; Lee, H. Estimation of the Effective Zone of Sea/Land Breeze in a Coastal Area. *Atmos. Pollut. Res.* **2011**, *2*, 106–115. [[CrossRef](#)]
42. Skamarock, C.; Klemp, B.; Dudhia, J.; Gill, O.; Barker, D.M.; Duda, G.; Huang, X.; Wang, W.; Powers, G. *A Description of the Advanced Research WRF Version 3*; University Corporation for Atmospheric Research: Boulder, CO, USA, 2008. [[CrossRef](#)]
43. Di, Z.; Gong, W.; Gan, Y.; Shen, C.; Duan, Q. Combinatorial Optimization for WRF Physical Parameterization Schemes: A Case Study of Three-Day Typhoon Simulations over the Northwest Pacific Ocean. *Atmosphere* **2019**, *10*, 233. [[CrossRef](#)]
44. Krieger, J.R.; Zhang, J.; Atkinson, D.E.; Zhang, X. Sensitivity of WRF Model Forecasts to Different Physical Parameterizations in the Beaufort Sea Region. In Proceedings of the 8th Conference on Coastal Atmospheric and Oceanic Prediction and Processes, San Diego, CA, USA, 10–15 January 2009.
45. Zhang, Y.; Sartelet, K.; Zhu, S.; Wang, W.; Wu, S.-Y.; Zhang, X.; Wang, K.; Tran, P.; Seigneur, C.; Wang, Z.-F. Application of WRF/Chem-MADRID and WRF/Polyphemus in Europe—Part 2: Evaluation of Chemical Concentrations and Sensitivity Simulations. *Atmos. Chem. Phys.* **2013**, *13*, 6845–6875. [[CrossRef](#)]
46. Nakanishi, M.; Niino, H. An Improved Mellor–Yamada Level-3 Model: Its Numerical Stability and Application to a Regional Prediction of Advection Fog. *Bound. Layer Meteorol.* **2006**, *119*, 397–407. [[CrossRef](#)]
47. Mellor, G.L.; Yamada, T. Development of a Turbulence Closure Model for Geophysical Fluid Problems. *Rev. Geophys.* **1982**, *20*, 851–875. [[CrossRef](#)]
48. Sukoriansky, S.; Galperin, B.; Perov, V. A Quasi-Normal Scale Elimination Model of Turbulence and Its Application to Stably Stratified Flows. *Nonlinear Process. Geophys.* **2006**, *13*, 9–22. [[CrossRef](#)]

49. Hong, S.-Y.; Noh, Y.; Dudhia, J. A New Vertical Diffusion Package with an Explicit Treatment of Entrainment Processes. *Mon. Weather Rev.* **2006**, *134*, 2318–2341. [CrossRef]
50. Pleim, J.E. A Combined Local and Nonlocal Closure Model for the Atmospheric Boundary Layer. Part I: Model Description and Testing. *J. Appl. Meteorol. Climatol.* **2007**, *46*, 1383–1395. [CrossRef]
51. Dudhia, J. Numerical Study of Convection Observed during the Winter Monsoon Experiment Using a Mesoscale Two-Dimensional Model. *J. Atmos. Sci.* **1989**, *46*, 3077–3107. [CrossRef]
52. Iacono, M.J.; Delamere, J.S.; Mlawer, E.J.; Shephard, M.W.; Clough, S.A.; Collins, W.D. Radiative Forcing by Longlived Greenhouse Gases: Calculations with the AER Radiative Transfer Models. *J. Geophys. Res.* **2008**, *113*, D13. [CrossRef]
53. Mlawer, E.J.; Taubman, S.J.; Brown, P.D.; Iacono, M.J.; Clough, S.A. Radiative Transfer for Inhomogeneous Atmospheres: RRTM, a Validated Correlated-k Model for the Longwave. *J. Geophys. Res.* **1997**, *102*, 16663–16682. [CrossRef]
54. Jiménez, P.A.; Dudhia, J.; Navarro, J. A Revised Scheme for the WRF Surface Layer Formulation. *Mon. Weather Rev.* **2012**, *140*, 898–918. [CrossRef]
55. Skamarock, W.C. Evaluating Mesoscale NWP Models Using Kinetic Energy Spectra. *Mon. Weather Rev.* **2004**, *132*, 3019–3032. [CrossRef]
56. Abida, R.; Attié, J.-L.; el Amraoui, L.; Ricaud, P.; Lahoz, W.; Eskes, H.; Segers, A.; Curier, L.; de Haan, J.; Kujanpää, J.; et al. Impact of Spaceborne Carbon Monoxide Observations from the S-5P Platform on tropospheric Composition Analyses and Forecasts. *Atmos. Chem. Phys.* **2017**, *17*, 1081–1103. [CrossRef]
57. Surussavadee, C. Evaluation of WRF Near-Surface Wind Simulations in Tropics Employing Different Planetary Boundary Layer Schemes. In Proceedings of the 2017 8th International Renewable Energy Congress (IREC), Amman, Jordan, 21–23 March 2017; pp. 1–4. [CrossRef]
58. Agostinelli, C.; Lund, U. R Package: Circular Statistics (Version 0.4-93). 2017. Available online: <https://R-Forge.r-Project.Org/Projects/Circular/> (accessed on 15 May 2022).
59. Gbode, I.E.; Dudhia, J.; Ogunjobi, K.O.; Ajayi, V.O. Sensitivity of Different Physics Schemes in the WRF Model during a West African Monsoon Regime. *Theor. Appl. Climatol.* **2018**, *136*, 733–751. [CrossRef]
60. Charnock, H. Wind Stress on a Water Surface. *Q. J. R. Meteorol. Soc.* **1955**, *81*, 639–640. [CrossRef]
61. Lee, J.A.; Hacker, J.P.; Monache, L.D.; Kosović, B.; Clifton, A.; Vandenberghe, F.; Rodrigo, J.S. Improving Wind Predictions in the Marine Atmospheric Boundary Layer Through Parameter Estimation in a Single Column Model. *Mon. Weather Rev.* **2017**, *145*, 5–24. [CrossRef]
62. Fonseca, R.; Temimi, M.; Thota, M.S.; Nelli, N.R.; Weston, M.J.; Suzuki, K.; Uchida, J.; Kumar, K.N.; Branch, O.; Wehbe, Y.; et al. On the Analysis of the Performance of WRF and NICAM in a Hyperarid Environment. *Weather Forecast.* **2020**, *35*, 891–919. [CrossRef]
63. Fonseca, R.; Francis, D.; Nelli, N.; Thota, M. Climatology of the Heat Low and the Intertropical Discontinuity in the Arabian Peninsula. *Int. J. Climatol.* **2022**, *42*, 1092–1117. [CrossRef]
64. Dumka, U.C.; Kaskaoutis, D.G.; Francis, D.; Chaboureau, J.-P.; Rashki, A.; Tiwari, S.; Singh, S.; Liakakou, E.; Mihalopoulos, N. The Role of the Intertropical Discontinuity Region and the Heat Low in Dust Emission and Transport Over the Thar Desert, India: A Premonsoon Case Study. *J. Geophys. Res. Atmos.* **2019**, *124*, 13197–13219. [CrossRef]
65. Nelli, N.; Fissehay, S.; Francis, D.; Fonseca, R.; Temimi, M.; Weston, M.; Abida, R.; Nesterov, O. Characteristics of Atmospheric Aerosols over the UAE Inferred from CALIPSO and Sun Photometer Aerosol Optical Depth. *Earth Space Sci. Open Arch.* **2020**, *37*, e2020EA001360. [CrossRef]
66. Branch, O.; Schwitalla, T.; Temimi, M.; Fonseca, R.; Nelli, N.; Weston, M.; Milovac, J.; Wulfmeyer, V. Seasonal and Diurnal Performance of Daily Forecasts with WRF V3.8.1 over the United Arab Emirates. *Geosci. Model Dev.* **2021**, *14*, 1615–1637. [CrossRef]
67. Borge, R.; Alexandrov, V.N.; del Vas, J.J.; Lumberras, J.; Rodriguez, E. A Comprehensive Sensitivity Analysis of the WRF Model for Air Quality Applications over the Iberian Peninsula. *Atmos. Environ.* **2008**, *42*, 8560–8574. [CrossRef]
68. Kwun, J.; Kim, Y.-K.; Seo, J.-W.; Jeong, J.-H.; You, S.H. Sensitivity of MM5 and WRF Mesoscale Model Predictions of Surface Winds in a Typhoon to Planetary Boundary Layer Parameterizations. *Nat. Hazards* **2009**, *51*, 63–77. [CrossRef]
69. Ruiz, J.; Saulo, C.; Nogués-Paegle, J. WRF Model Sensitivity to Choice of Parameterization over South America: Validation against Surface Variables. *Mon. Weather Rev.* **2010**, *138*, 3342–3355. [CrossRef]
70. García-Díez, M.; Fernández, J.; Fita, L.; Yagüe, C. Seasonal Dependence of WRF Model Biases and Sensitivity to PBL Schemes over Europe. *Q. J. R. Meteorol. Soc.* **2013**, *139*, 501–514. [CrossRef]
71. Weston, M.; Chaouch, N.; Valappil, V.; Temimi, M.; Ek, M.; Zheng, W. Assessment of the Sensitivity to the Thermal Roughness Length in Noah and Noah-MP Land Surface Model Using WRF in an Arid Region. *Pure Appl. Geophys.* **2019**, *176*, 2121–2137. [CrossRef]